



Published in final edited form as:

*Nat Struct Mol Biol.* 2019 December ; 26(12): 1123–1131. doi:10.1038/s41594-019-0330-y.

## Structure of an Endosomal Signaling GPCR–G Protein– $\beta$ -arrestin Mega-Complex

Anthony H. Nguyen<sup>1,2,†</sup>, Alex R. B. Thomsen<sup>1,3,†</sup>, Thomas J. Cahill III<sup>1,2,†</sup>, Rick Huang<sup>4</sup>, Li-Yin Huang<sup>1</sup>, Tara Marcink<sup>6,7</sup>, Oliver B. Clarke<sup>8,9,10</sup>, Søren Heissel<sup>11</sup>, Ali Masoudi<sup>1</sup>, Danya Ben-Hail<sup>5</sup>, Fadi Samaan<sup>5</sup>, Venkata P. Dandey<sup>12</sup>, Yong Zi Tan<sup>12,13</sup>, Chuan Hong<sup>4</sup>, Jacob P. Mahoney<sup>14,15</sup>, Sarah Triest<sup>16</sup>, John Little IV<sup>2</sup>, Xin Chen<sup>17</sup>, Roger Sunahara<sup>14,18</sup>, Jan Steyaert<sup>16</sup>, Henrik Molina<sup>11</sup>, Zhiheng Yu<sup>4</sup>, Amedee des Georges<sup>5,19,20,\*</sup>, Robert J. Lefkowitz<sup>1,2,21,\*</sup>

<sup>1</sup>Department of Medicine, Duke University Medical Center, Durham, NC 27710, USA.

<sup>2</sup>Department of Biochemistry, Duke University Medical Center, Durham, NC 27710, USA.

<sup>3</sup>Department of Surgery, Columbia University Irving Medical Center, New York, NY 10032, USA.

<sup>4</sup>Howard Hughes Medical Institute, Janelia Research Campus, Ashburn, VA 20147, USA.

<sup>5</sup>Structural Biology Initiative, CUNY Advanced Science Research Center, NY 10031, USA

<sup>6</sup>Department of Pediatrics, Columbia University Irving Medical Center, New York, NY 10032, USA.

<sup>7</sup>Center for Host-Pathogen Interaction, Columbia University Irving Medical Center, New York, NY 10032, USA.

<sup>8</sup>Department of Anesthesiology, Columbia University Irving Medical Center, New York, NY 10032, USA.

<sup>9</sup>Department of Physiology and Cellular Biophysics, Columbia University Irving Medical Center, New York, NY 10032, USA.

<sup>10</sup>The Irving Center for Clinical and Translational Research, Columbia University Irving Medical Center, New York, NY 10032, USA.

<sup>11</sup>Proteomics Resource Center, The Rockefeller University, New York, New York 10065, USA.

Users may view, print, copy, and download text and data-mine the content in such documents, for the purposes of academic research, subject always to the full Conditions of use:[http://www.nature.com/authors/editorial\\_policies/license.html#terms](http://www.nature.com/authors/editorial_policies/license.html#terms)

\*Corresponding authors: [adesgeorges@gc.cuny.edu](mailto:adesgeorges@gc.cuny.edu) (A.d.G.); [lefko001@receptor-biol.duke.edu](mailto:lefko001@receptor-biol.duke.edu) (R.J.L.).

†These authors contributed equally to this work.

### Author Contributions

A.H.N., A.R.B.T., T.J.C III, A.d.G., and R.J.L. conceived the project and designed experimental approaches. A.H.N., A.R.B.T., T.J.C III, L.-Y.H., A. M., J.P.M., J.L.IV and R.S. purified protein for cryo-EM structural determination. A.H.N. prepared cryo-EM samples with contribution from V.P.D. A.H.N., A.R.B.T., T.J.C III, D.B.-H., F.S. and A.d.G. performed initial sample screenings. R.H. and Z.Y. performed cryo-EM imaging with contributions from C.H. A.H.N. processed cryo-EM data with input from A.d.G. and Y.Z.T. A.H.N. and O.B.C. built the atomic models. S.T. and J.S. raised Nanobody 32, and X.C. synthesized BI-167107. S.H. and H.M. performed LC-MS/MS experiments and data analyses. T.M. performed coarse-grained molecular dynamics analysis. A.R.B.T. performed real-time cellular cAMP measurement experiments. A.H.N., A.R.B.T., T.J.C III, A.d.G., and R.J.L. interpreted the data and wrote the manuscript. R.J.L. and A.d.G. were responsible for project supervision and management.

### Competing Interests Statement

The authors declare no competing interests.

<sup>12</sup>The National Resource for Automated Molecular Microscopy, Simons Electron Microscopy Center, New York Structural Biology Center, New York, NY 10027, USA

<sup>13</sup>Department of Biochemistry and Molecular Biophysics, Columbia University Irving Medical Center, New York, NY 10032, USA

<sup>14</sup>Department of Pharmacology, University of Michigan, Ann Arbor, MI 48109, USA

<sup>15</sup>Present Address: Department of Structural Biology, Stanford University, Stanford, CA

<sup>16</sup>Structural Biology Brussels, Vrije Universiteit Brussels, B-1050 Brussels, Belgium; Structural Biology Research Center, Vlaams Instituut voor Biotechnologie, B-1050 Brussels, Belgium.

<sup>17</sup>School of Pharmaceutical Engineering and Life Sciences, Changzhou University, Changzhou, Jiangsu 213164, China.

<sup>18</sup>Department of Pharmacology, University of California, San Diego, La Jolla, CA 92093, USA.

<sup>19</sup>Department of Chemistry and Biochemistry, City College of New York, NY, USA

<sup>20</sup>Biochemistry and Chemistry Ph.D. Programs, Graduate Center, City University of New York, NY, USA

<sup>21</sup>Howard Hughes Medical Institute, Duke University Medical Center, Durham, NC 27710, USA.

## Abstract

Classically, G protein-coupled receptors (GPCRs) are thought to activate G protein from the plasma membrane and are subsequently desensitized by  $\beta$ -arrestin ( $\beta$ arr). However, some GPCRs continue to signal through G protein from internalized compartments, mediated by a GPCR–G protein– $\beta$ arr ‘megaplex’. Nevertheless, the megaplex’s molecular architecture remains unknown. Here, we present its cryo-electron microscopy structure, which shows simultaneous engagement of human G protein and bovine  $\beta$ arr to the core and phosphorylated tail, respectively, of a single active human chimeric  $\beta_2$ -adrenergic receptor with the C-terminal tail of the arginine vasopressin type 2 receptor ( $\beta_2V_2R$ ). All three components adopt their canonical active conformations, suggesting that a single megaplex GPCR is capable of simultaneously activating G protein and  $\beta$ arr. Our findings provide a structural basis for GPCR-mediated sustained, internalized G protein signaling.

---

G protein coupled receptors (GPCRs) are a class of ubiquitous cell-surface receptors involved in the regulation of many physiological processes<sup>1,2</sup>. An agonist stabilizes a GPCR in an active conformation, which facilitates binding and activation of G proteins. This leads to generation of second messenger molecules like cyclic AMP (cAMP) and subsequent signal propagation. In order to terminate G protein signaling, GPCR kinases (GRKs) phosphorylate the receptor, often on its C-terminal tail, which enables binding of  $\beta$ -arrestin ( $\beta$ arr) to the receptor<sup>1,3</sup>.  $\beta$ arr interacts with both the phosphorylated GPCR tail and intracellular core, with the latter interaction sterically blocking G protein binding and desensitizing further G protein signaling.  $\beta$ arr promotes internalization of the receptor by recruiting endocytic proteins (Fig. 1)<sup>3,4</sup>. Subsequently, the receptor is either: 1) rapidly recycled to the plasma membrane for receptors that transiently interact with  $\beta$ arr (class A GPCRs) or 2) internalized into endosomes followed by degradation for receptors that

strongly interact with  $\beta$ arr (class B GPCRs)<sup>4,5</sup>.  $\beta$ arr is also capable of mediating G protein-independent signaling pathways by scaffolding other signaling proteins<sup>3</sup>.

Recently, class B GPCRs such as the thyroid-stimulating hormone receptor, parathyroid hormone receptor and the vasopressin type 2 receptor ( $V_2R$ ) have been reported to engage in sustained G protein signaling after receptor internalization into endosomes rather than being desensitized<sup>6-9</sup>. Internalized G protein signaling has been difficult to incorporate within the 'classical understanding' of GPCR biology, since the GPCR- $\beta$ arr interaction which drives internalization was thought to sterically block G protein binding and desensitize further signaling. However, we demonstrated that GPCR- $\beta$ arr complexes can assume two distinct conformations with  $\beta$ arr either: (1) only bound to the phosphorylated receptor C-terminal tail and appears to hang from the receptor ('tail conformation'); or (2) also bound concurrently to the receptor intracellular core via its finger loop region ('core conformation')<sup>9-11</sup>. In the tail conformation, the receptor intracellular core is presumably exposed, potentially allowing for interaction with G protein to form a GPCR-G protein- $\beta$ arr 'megaplex' capable of stimulating G protein signaling while being internalized by  $\beta$ arr (Fig. 1, black box)<sup>9</sup>.

The megaplex hypothesis is supported by the observation that megaplex components come into close proximity with each other at endosomes for many class B GPCRs using cellular bioluminescence resonance energy transfer (BRET) assays<sup>6,8,9,12-14</sup>. Additionally, we previously demonstrated that functional megaplexes can be formed *in vitro* in an agonist-dependent manner, and the GPCRs within these megaplexes activate G proteins by promoting GTPase activity, GTP/GDP exchange and dissociation of the  $G\alpha$  subunit from  $G\beta\gamma$  subunits<sup>9</sup>.

That a GPCR within a megaplex can elicit both G protein and  $\beta$ arr functions (i.e. internalization) raises a number of questions: what is the conformation of a GPCR when simultaneously bound to both G protein and  $\beta$ arr? What are the conformations of the megaplex  $\beta$ arr and G protein, and how do these conformations compare to the canonical active conformations they each separately adopt? To answer these questions and understand the structural basis for megaplex-mediated signaling by internalized GPCRs, we here report a cryo-electron microscopy (cryo-EM) structure of the megaplex.

## Results

### Complex Formation and Structure Solution

To form megaplexes, we first purified the  $\beta_2V_2R$ - $\beta$ arr complex co-expressed with a prenylated GRK2 (GRK2-CAAX) bound to the high-affinity  $\beta_2$ -adrenergic receptor ( $\beta_2AR$ ) agonist BI-167107 (BI) and stabilized by the conformationally sensitive antibody fragment Fab30<sup>10</sup>. Gs protein was added to the  $\beta_2V_2R$ - $\beta$ arr1-Fab30 complex to form the megaplex along with nanobody 35 (Nb35) to stabilize the  $\beta_2V_2R$ -Gs interaction (Extended Data Fig. 1)<sup>9,15</sup>. The  $\beta_2V_2R$  is an N-terminal T4 lysozyme (T4L)-fused, modified  $\beta_2AR$  with the first 341 residues of the  $\beta_2AR$  combined with the last 29 amino acids  $V_2R$  C-terminal tail ( $V_2T$ )<sup>10</sup>. While maintaining the pharmacological properties of the  $\beta_2AR$ , the  $\beta_2V_2R$

interacts strongly with  $\beta$ arrs, forming megaplexes and promotes endosomal G protein signaling comparable to the class B  $V_2R^{4,5,9-11}$ .

Initial cryo-EM imaging revealed significant dissociation of the megaplex, with class averages from the few intact megaplex particles displaying preferential orientation and blurred density for the  $\beta$ arr1–Fab30 portion, presumably due to its flexibility (Extended Data Fig. 2). To improve complex stability, we formed the megaplex with Nanobody 32 (Nb32), which further stabilizes active  $\beta$ arr1 bound to the phosphorylated  $V_2T^{11}$ . Nb32 substantially enhanced the number of intact megaplex particles and led to better-defined density for  $\beta$ arr1–Fab30 in class averages, potentially by sterically limiting  $\beta$ arr1–Fab30 flexibility (Extended Data Fig. 2). To overcome preferential orientation, all data were subsequently collected with the specimen stage tilted from  $30^\circ$  to  $50^\circ$  (Extended Data Figs. 3,4).

Our initial reconstruction of the megaplex shows Gs binding to the  $\beta_2V_2R$  intracellular core, while  $\beta$ arr1 binds to the phosphorylated  $V_2T$  in a tail conformation (Extended Data Fig. 5). We do not observe additional contact between  $\beta$ arr1 and the receptor, nor any direct contact between Gs and  $\beta$ arr1 (Extended Data Fig. 5). We observe Nb32 binding to the N-terminal lobe of  $\beta$ arr1, and that it sterically makes contact with the  $\beta_2V_2R$  and Nb35 at low map thresholds (Extended Data Fig. 5).

The phosphorylated receptor C-terminal tail serves as the only connection between the receptor and  $\beta$ arr1. Because this connection is inherently flexible, our structure's local resolution is limited to  $\sim 7 \text{ \AA}$  (Extended Data Figs. 5,6). Subsequent attempts to reconstruct the megaplex after computationally subtracting Fab30 and Nb32 densities led to a map with well-defined features for the  $\beta_2V_2R$ –Gs–Nb35 portion, but not for the smaller  $\beta$ arr1 bound to the phosphorylated tail, indicating that  $\beta$ arr1 is truly flexible relative to the  $\beta_2V_2R$ –Gs–Nb35 component (Extended Data Fig. 4).

To overcome this inherent flexibility, we analyzed the megaplex as two separate subcomplexes: the BI– $\beta_2V_2R$ –Gs–Nb35 (with T4L removed) and the Nb32– $V_2T$ – $\beta$ arr1–Fab30 subcomplexes, from this point on referred to as the  $\beta_2V_2R$ –Gs and  $\beta$ arr1– $V_2T$  subcomplexes, respectively. By realigning each subcomplexes separately, we obtained reconstructions for the  $\beta_2V_2R$ –Gs and  $\beta$ arr1– $V_2T$  subcomplexes at  $3.8 \text{ \AA}$  and  $4.0 \text{ \AA}$ , respectively (Table 1, and Extended Data Figs. 4, 6, 7). While the subcomplexes' resolution vary directionally, the higher resolution allows for analysis of all relevant megaplex interactions. These subcomplex reconstructions are aligned to the overall reconstruction and displayed together as a composite cryo-EM map (Fig. 2a,b).

### The $\beta_2V_2R$ –Gs portion of the megaplex

The Gs protein engages the  $\beta_2V_2R$  at its intracellular core (Fig. 3a). To assess the megaplex  $\beta_2V_2R$  conformation, we compared it to the structures of inactive, carazolol-bound  $\beta_2AR$  (PDB: 2RH1) and the active, Gs protein-bound  $\beta_2AR$  (PDB: 3SN6)<sup>15,16</sup>. In comparison to the inactive  $\beta_2AR$  structure, the megaplex  $\beta_2V_2R$  shows a  $15 \text{ \AA}$  outward shift away from the receptor intracellular core in its transmembrane (TM) helix 6, as measured from the Ca of residue E268<sup>6,30</sup> (superscript denotes Ballesteros-Weinstein numbering)<sup>17</sup>. TM5 displays an

outward movement of 3 Å, as measured from the C $\alpha$  of L230<sup>5,69</sup>. TM3 and TM7 move inward towards the intracellular core by 2 Å (as measured from T136<sup>3,55</sup>) and 5 Å (as measured from C327<sup>7,54</sup>), respectively (Fig. 3b). These changes are consistent with those observed in the active, Gs-bound  $\beta_2$ AR<sup>15</sup>. The Gs-bound  $\beta_2$ AR and our  $\beta_2$ V<sub>2</sub>R are nearly superimposable, with a C $\alpha$  RMSD of 0.63 Å (Fig. 3c). Examination of the ligand binding pocket reveals density that can be attributed to BI, which adopts a similar binding pose to those in previous crystal structures of BI-occupied  $\beta_2$ AR bound to G protein-mimicking nanobodies (Fig. 3d, and Extended Data Fig. 8a)<sup>18,19</sup>.

Analysis of the  $\beta_2$ V<sub>2</sub>R–Gs interaction surface revealed contacts mostly between the  $\alpha$ 5 helix on G $\alpha$ s and TM3, TM5, TM6, and intracellular loop 2 (ICL2), consistent with those observed in the  $\beta_2$ AR–Gs crystal structure (Fig. 3e). The G $\alpha$ s  $\alpha$ 5 helix forms primarily nonpolar interactions with various residues located in TM5 and TM6 (Fig. 3e, and Extended Data Fig. 8b). Polar residues on TM5 of the receptor, namely E225<sup>5,64</sup>, Q229<sup>5,68</sup>, and K232<sup>5,71</sup>, are within distance to form a hydrogen bonding network with G $\alpha$ s residues D381 and Q384. Also notable is the nonpolar interaction formed between F139<sup>34,51</sup> in ICL2 with the hydrophobic pocket formed by V217, F219, and F376 of G $\alpha$ s (Fig. 3e, and Extended Data Fig. 8b). Significant interactions involving the DRY motif, namely packing of Y391 of the G $\alpha$ s  $\alpha$ 5 helix against R131<sup>3,50</sup> as well as the hydrogen bonding network between Y141<sup>34,53</sup>, T68<sup>2,39</sup>, and D130<sup>3,49</sup> is also observed (Fig. 3e, and Extended Data Fig. 8b).

In the presence of the tail-bound  $\beta$ arr1, when our  $\beta_2$ V<sub>2</sub>R–Gs and the  $\beta_2$ AR–Gs complex were aligned by their receptors, a 3.4° rotation in G $\beta\gamma$  around an axis parallel to the membrane was observed, and a 3° rotation in G $\alpha$ s was observed around an axis parallel to the  $\beta_2$ V<sub>2</sub>R–G $\alpha$ s contact compared to the  $\beta_2$ AR–Gs crystal structure (Fig. 3f). Taken together, while G protein adopts a distinct rotational pose, the overall receptor conformation and key receptor–Gs interactions appear to be unchanged, suggesting canonical G protein activation by a megaplex GPCR.

### The $\beta$ arr1–V<sub>2</sub>T portion of the megaplex

The  $\beta$ arr1–V<sub>2</sub>T subcomplex shows V<sub>2</sub>T binding to the N-terminal lobe of an active  $\beta$ arr1, indicated by a ~20° twist between its N and C-terminal lobes (Fig. 4a). Fab30 and Nb32 concurrently interact with various regions of  $\beta$ arr1 as well as the V<sub>2</sub>T; Fab30 forms hydrogen bonds with phosphorylated residues S362 (pS362) while Nb32 forms electrostatic interactions with pS363 and pS364 on the V<sub>2</sub>T (Extended Data Fig. 9a,b). The direct interactions of Fab30 and Nb32 with the V<sub>2</sub>T provide an explanation for the conformational selectivity of these stabilizers for active  $\beta$ arr.

Previously, we reported a crystal structure of a Fab30-stabilized  $\beta$ arr1 bound to a synthetic V<sub>2</sub>R phosphopeptide (V<sub>2</sub>Rpp), which acts as a phosphorylated receptor C-terminal tail mimic<sup>20</sup>. The V<sub>2</sub>Rpp is derived from the last 29 amino acids of the V<sub>2</sub>R and contains eight chemically synthesized potential phosphorylated serines and threonines at positions pT347, pS350, pS357, pT359, pT360, pS362, pS363, and pS364. However, our structure shows only six GRK2-phosphorylated residues on the V<sub>2</sub>T that interact with  $\beta$ arr1: pS357, pT359, pT360, pS362, pS363, and pS364 (Fig. 4b,c and Extended Data Fig. 10a).

All of these phosphorylated residues with the exception of pT359 form electrostatic interactions with lysines and arginines lining the surface of the N-terminal lobe of  $\beta$ arr1. Residue pT359 points outward and does not appear to make any contact with  $\beta$ arr1 (Fig. 4b). More specifically, residues pS357 and pS363 make electrostatic interactions with the well-conserved  $\beta$ arr1 residues K11 and K10 within  $\beta$ -strand I of  $\beta$ arr1, respectively (Fig. 4b). In addition, both pS363 and pS364 appear to interact with K107 on  $\alpha$ -helix I of  $\beta$ arr1, while pS362 is positioned to interact with R7 (Fig. 4c). Finally, pT360 is well-positioned to interact with R25 and K294. These interactions are comparable with interactions previously reported between the  $V_2$ Rpp and  $\beta$ arr1<sup>20</sup>.

A comparison between the  $\beta$ arr1- $V_2$ T subcomplex and the  $V_2$ Rpp- $\beta$ arr1-Fab30 crystal structure illustrates that while  $\beta$ arr1 in both structures adopts a similar active conformation (Ca RMSD of 0.76Å), the structure with  $V_2$ Rpp contains interaction between pS347 and pT350 not observed in our structure (Fig. 5a). pS347 interacts extensively with residues on  $\beta$ arr1 near the finger loop' region, forming ionic interactions with R65 and K77 and participates in hydrogen bonding with Y63. Similarly, pT350 forms electrostatic interactions with R62, K138, and R165 on  $\beta$ arr1 (Fig. 5a, inset).

To gain further insight into which serine and threonine residues on the  $V_2$ T are phosphorylated upon receptor stimulation, we performed liquid chromatography-tandem mass spectrometry (LC-MS/MS) on unstimulated  $\beta_2V_2R$  expressed by itself and BI-stimulated  $\beta_2V_2R$  co-expressed with GRK2-CAAX (Extended Data Fig. 10b). Our analysis revealed that T347, S350, S363, and S364 are phosphorylated in both samples, whereas S357, T359, T360, and S362 are only phosphorylated after receptor stimulation. These data suggest that: (1) T347/S350 are phosphorylated independent of stimulation, potentially through a GRK-independent mechanism and are not critical for  $\beta$ arr1 binding, (2) phosphorylation at residues S357, T359, T360, and S362 are necessary to recruit and stabilize  $\beta$ arr1 interaction with the  $V_2$ T.

Finally, from our EM map, we observe an additional interaction between two acidic  $V_2$ T residues D355 and E356 with  $\beta$ arr1, not observed in the  $V_2$ Rpp- $\beta$ arr1-Fab30 crystal structure (Fig. 4c). While local resolution does not allow for placement of side chains for D355 and E356, cryo-EM density for this region suggests that they are in position to interact with K160 and R161 on  $\beta$ arr1. Interestingly, these two acidic residues are prevalent in the C-terminal tail of a number of GPCRs (e.g.  $\beta_2$ AR, rhodopsin, and vasopressin receptors) and have been proposed to form a consensus motif for GRK1 and GRK2 phosphorylation, which when mutated in the closely-related vasopressin 1a receptor led to a loss in all tail phosphorylation<sup>21</sup>.

In order to further understand the structural implications of GPCR-arrestin interaction, we compared our  $\beta$ arr1- $V_2$ T portion of the megaplex, which binds to the  $\beta_2V_2R$  in a tail conformation, to the rhodopsin-visual arrestin crystal structure, in which visual arrestin binds the intracellular core of rhodopsin in addition to the phosphorylated tail (Fig. 5b). Alignment of  $\beta$ arr1 and visual arrestin in these two structures show that  $V_2$ T residues pS357, pT360, pS363 align well with residues pT336, pS338, and E341 on the rhodopsin tail. In addition, our structure has three additional phosphorylation sites, at positions pT359,

pS362, and pS364 (Fig. 5b). All of these additional sites, with the exception of pT359, interact with  $\beta$ arr1, most likely conferring higher receptor affinity to  $\beta$ arr1 even though a smaller number of phosphorylated residues on a GPCR tail may be sufficient to activate arrestin.

### Architecture of the megaplex within a cell membrane

We noted that  $\beta$ arr1 in our megaplex structure is pointing upward towards an area where the membrane is located in a cellular context. This position of  $\beta$ arr1 is facilitated by a physical clash between the receptor, Nb35 and Nb32, both of which are needed to stabilize the complex, and the lack of a membranous barrier in our detergent-purified megaplex (Extended Data Fig. 5). Therefore, we employed coarse-grained molecular dynamics (MD) simulation to explore the movement of  $\beta$ arr1 when bound to the highly flexible receptor C-terminal tail within the megaplex in a cellular environment.

We modeled the entire megaplex embedded within a dipalmitolphosphatidylcholine (DPPC) bilayer in the absence of all protein stabilizers (Fig. 6a). As expected,  $\beta$ arr1 movement is much more constrained when a lipid bilayer is present. Moreover, the two proline residues 348 and 349 induces a kink in the  $V_2T$ , thus serves to restrict  $\beta$ arr1 distance from the  $\beta_2V_2R$ -Gs portion. Even though these two factors limit the  $\beta$ arr1 range of motion, it can still adopt a wide range of possible conformations. To sample this conformational range, we modeled three possible megaplex structures, each of them different by the position of  $\beta$ arr1- $V_2T$  in relation to the  $\beta_2V_2R$ -Gs portion and the membrane (Fig. 6a, MD runs 1-3). A 30 ns coarse-grained MD simulation was run using each modeled structure as a starting point (Fig. 6b). In all three MD runs,  $\beta$ arr1 flexibly moves in relation to the  $\beta_2V_2R$ -Gs subcomplex. Interestingly, in runs 1 and 3, nonpolar  $\beta$ arr1 residues <sup>332</sup>GLLG<sup>336</sup>, part of a loop at the distal edge of the C-terminal lobe, make transient contacts with the lipid bilayer at various time points (Fig. 6b, black circles). Another  $\beta$ arr1 C-terminal loop, comprising residues <sup>261</sup>TVAPS<sup>265</sup>, also makes contact with the membrane, albeit to a lesser extent. Previous MD experiments as well as the rhodopsin-visual arrestin crystal structure (in which visual arrestin binds both the phosphorylated C-terminal tail and core of rhodopsin) have both shown that various analogous loops in visual arrestin can interact with a lipid bilayer<sup>22,23</sup>. Our results indicate that a tail-bound  $\beta$ arr1 in a megaplex has the ability to maintain this interaction, and further highlight the diverse positions that  $\beta$ arr1 could adopt within the cell membrane as part of the megaplex.

The ability of  $\beta_2V_2R$  to interact with and activate Gs while being bound to  $\beta$ arr1 through the flexible C-terminal tail in a cellular context was further confirmed using  $\beta$ arr1/ $\beta$ arr2/ $\beta_2AR$  triple knock-out HEK293 cells transiently expressing functionally verified  $\beta_2V_2R$ - $\beta$ arr1 or  $\beta_2V_2R$ - $\beta$ arr2 fusion proteins<sup>9,11</sup>. In these cells, BI-stimulation of  $\beta_2V_2R$ - $\beta$ arr1/2 resulted in a fast and sustained increase in cAMP comparable to either  $\beta_2V_2R$  alone or forskolin-stimulated cAMP production (Fig. 6c). These results demonstrate that a single GPCR residing within a cell membrane and while being coupled functionally to  $\beta$ arr (in this case through a covalent attachment) can still physically interact with and activate G protein.

## Discussion

The initial discovery of  $\beta$ arrs provided a mechanism for how GPCR-mediated G protein signaling is desensitized<sup>24,25</sup>. Overlapping binding sites of G proteins and  $\beta$ arrs at the receptor core have been confirmed in multiple structural studies, and therefore, it has traditionally been assumed that binding of G protein and  $\beta$ arr to a single receptor are mutually exclusive<sup>15,23–28</sup>.

However, the discovery that a class B GPCR– $\beta$ arr complex in the tail conformation can continue to activate G protein through the formation of megaplexes provides a biophysical explanation for the ability of some GPCRs to signal within internalized cellular compartments. Now, we show in our megaplex structure that the BI-bound, active  $\beta_2V_2R$  binds to Gs protein at the receptor intracellular core while coupling to  $\beta$ arr1 via the phosphorylated V<sub>2</sub>T (Fig. 2). The  $\beta_2V_2R$ –Gs contacts in the megaplex are also comparable to those of the  $\beta_2AR$ –Gs structure, indicating that Gs protein is being activated by the megaplex receptor in a canonical fashion (Fig. 3e). The V<sub>2</sub>T-bound  $\beta$ arr1 also adopts an active conformation, indicated by  $\sim 20^\circ$  twisting of its N and C-terminal lobes (Fig. 4a). The structure demonstrates that the binding of G protein and  $\beta$ arr to the same GPCR are not mutually exclusive, with both transducers being canonically activated.

Verified by LC-MS/MS analyses, six phosphorylated residues were visualized on the GPCR tail, with five of them engaging the active megaplex  $\beta$ arr1 (Fig. 4, and Extended Data Fig. 10b). These observations further recapitulate cellular data that demonstrate decrease in phosphorylation and, by extension, arrestin recruitment to the GPCR after mutating one or a series of these phosphorylated residues<sup>4,23,29,30</sup>. A recent biochemical study showed V<sub>2</sub>R phosphopeptides which contained more phosphorylated residues bind  $\beta$ arr with much higher affinity<sup>31</sup>. Therefore, the presence of multiple phosphorylated residues on the V<sub>2</sub>T likely enhances the affinity of  $\beta_2V_2R$ – $\beta$ arr1 interaction and thus contributes to megaplex formation. Moreover, our LC-MS/MS results suggest that while some residues are phosphorylated independent of receptor stimulation, specific phosphorylation sites are necessary to recruit and stabilize  $\beta$ arr1 on the GPCR tail (Extended Data Fig. 10b).

Oriental changes in receptor-bound G proteins have been implicated in downstream signaling consequences, as can be observed with previous structures of comparable GPCRs in the presence of differing ligands or receptor binders<sup>27,28,32,33</sup>. In the presence of  $\beta$ arr, the G $\alpha$ s subunit within the megaplex displays a  $3^\circ$  rotation by an axis parallel to the  $\beta_2V_2R$ –Gs contact. Additionally, the G $\beta\gamma$  subunits displays a  $3.4^\circ$  rotation by an axis parallel to the membrane, potentially as a consequence of  $\beta$ arr1 binding to the V<sub>2</sub>T (Figure 3f).

MD experiments reveal a flexible megaplex  $\beta$ arr1 capable of adopting multiple positions in relation to the  $\beta_2V_2R$ –Gs subcomplex, and hints at transient contacts made between nonpolar  $\beta$ arr1 edge residues and the membrane. Comparable C-edge loops within visual arrestin have also been shown to interact with the lipid bilayer when bound to an active rhodopsin<sup>22,23</sup>. Recently, our group has also demonstrated that the tail conformation of a GPCR– $\beta$ arr complex is capable of signaling, raising an interesting possibility that a

megaplex  $\beta$ arr can also signal within internalized compartments by binding to downstream effectors<sup>11</sup>.

We observed an interaction between V<sub>2</sub>T residues D355 and E356 and  $\beta$ arr1 (presumably at K160 and R161) in the megaplex structure. This interaction is analogous to one observed between two acidic rhodopsin C-terminal tail residues, D330 and E332, and visual arrestin residues R19, K167, and K168. Along with the binding of rhodopsin C-terminal tail residue E341 to visual arrestin, these observations suggest that acidic residues, in addition to phosphorylated residues, play an important role in the association of arrestin by the C-terminal tail of a GPCR.

The fact that class B GPCRs primarily signal in a prolonged manner implicates the tail conformation in propagating sustained signaling. This is further reinforced by the fact that class A GPCRs like the  $\beta_2$ AR, which do not tightly associate with  $\beta$ arr, do not signal from internalized compartments or do so only weakly<sup>9,34</sup>. There are two potential ways in which  $\beta$ arr may enable a GPCR to continue G protein signaling: (1) by keeping the receptor internalized, and (2) by scaffolding free G $\beta\gamma$  to accelerate reassociation of GDP-bound G $\alpha_s$ , reforming a Gs heterotrimer that is in close proximity to a receptor-arrestin complex to initiate another round of signaling.

$\beta$ arr seems to serve as a scaffold for G $\beta\gamma$ , and together they have been shown to form a complex with a GPCR<sup>9,12,35</sup>. We have reported that the direct interaction between G $\beta\gamma$  subunits and phosphopeptide-bound active  $\beta$ arr1 increases upon Gs activation and separation of the G $\alpha_s$  from the G $\beta\gamma$  subunits<sup>9</sup>. Thus, it is possible that the interface of G $\beta\gamma$  subunits that associate with G $\alpha_s$  in the heterotrimeric Gs may interact with  $\beta$ arr1 upon Gs activation and G $\alpha_s$  separation. Indeed, currently available structures of G $\beta\gamma$  bound to protein effectors all show G $\beta\gamma$  interacting with them on the G $\beta$  interface that normally interacts with G $\alpha$ , consistent with the notion that G $\beta\gamma$  typically binds to other proteins after receptor-mediated dissociation from G $\alpha$ <sup>36–38</sup>. Such a G $\beta\gamma$  scaffolding role of  $\beta$ arrs may serve to confine the G protein near the receptor, resulting in an increased G protein activation rate from internalized compartments.

Our structure of the  $\beta_2$ V<sub>2</sub>R–Gs protein– $\beta$ arr1 megaplex shows an active, ligand-bound receptor simultaneously engaging Gs protein by its intracellular core and activating  $\beta$ arr1 via six phosphorylated residues in the receptor C-terminal tail. That the receptor is in an active conformation, contacts Gs in a canonical fashion, while allowing  $\beta$ arr1 to bind to its phosphorylated C-terminal tail points to the GPCR as a master regulator of signaling capable of activating G protein in addition to performing  $\beta$ arr-mediated signaling concurrently. Finally, our structure provides a biophysical basis for G protein activation and sustained signaling within internalized cellular compartments.

## Methods

### Purification of the T4L- $\beta_2$ V<sub>2</sub>R- $\beta$ arr1-Fab30 Complex, Gs Protein, and Protein Stabilizers

Gs protein, Fab30, and Nb32 were purified as previously described<sup>11,15,20</sup>. The T4L- $\beta_2$ V<sub>2</sub>R- $\beta$ arr1-Fab30 complex is also purified as previously described<sup>4</sup>. Briefly, *Sf9* cells

were co-expressed with T4L- $\beta_2V_2R$ , untagged bovine  $\beta$ arr1 (1–393), and GRK2-CAAX. Sixty-six hours post-infection, cells were stimulated for 30 minutes at 37 °C with 0.5  $\mu$ M BI-167107 to stimulate receptor phosphorylation and complex formation. After harvest, cells were resuspended and dounce-homogenized in 20 mM HEPES, 150 mM NaCl, pH 7.4, 100 nM BI, leupeptin-benzamidine (LB) protease inhibitor. Excess purified Fab30 were added to stabilize the complex, and the mixture was stirred for 30 minutes at RT. Subsequently, complexes were solubilized with the addition of 0.5% lauryl maltose neopentyl glycol (LMNG)/0.05% cholesteryl hemisuccinate (CHS) and the mixture was stirred for an additional hour. Cell debris were clarified by centrifugation and solubilized material were purified using M1 Anti-Flag resin. Complexes were subjected to a cysteine alkylation procedure as previously reported, concentrated using a 100 kDa-cutoff Millipore concentrator and loaded onto a size exclusion column (Extended Data Fig. 1)<sup>10</sup>. The purified complexes were flash frozen with glycerol and stored until further use.

### Formation of the Megaplex

In order to form megaplexes, the  $\beta_2V_2R$ - $\beta$ arr1-Fab30 complex was incubated with excess Gs protein, Nb35, and Nb32 at RT for 1 hr in 20 mM HEPES, 150 mM NaCl, pH 7.4, 4 mM CaCl<sub>2</sub>, 0.01% LMNG, and 30  $\mu$ M BI. Apyrase (25 mU/mL) was then added to the mixture and incubated at RT for 1 hr (Extended Data Fig. 1). To pull down megaplexes, M1 beads were added with subsequent incubation for an additional hour at RT. The beads were then spun down and washed five times with 20 mM HEPES, 150 mM NaCl, pH 7.4, 2 mM CaCl<sub>2</sub>, 0.01% LMNG, and 10  $\mu$ M BI. Finally, the megaplexes were eluted with buffer containing 20 mM HEPES, 100 mM NaCl, pH 7.4, 0.01% LMNG, 30  $\mu$ M BI, 0.2 mg/ml FLAG peptide, 1 mM TCEP, leupeptin-benzamidine protease inhibitor and 5 mM EDTA.

Initial samples were prepared in an identical manner without the use of Nb32.

### Cryo-EM Sample Preparation and Data Acquisition

For grid preparation, megaplex samples were used either at a concentration of 0.8 mg/ml or diluted to 0.4 mg/ml with the same elution buffer as described above. Three  $\mu$ L of the sample was applied to freshly glow-discharged UltrAufoil 0.6/1 300-mesh grids (Quantifoil, Großlobichau, Germany). The grids were prepared on an FEI Vitrobot Mark IV, blotted for 1.5 sec, and vitrified by plunge freezing into liquid ethane cooled by liquid nitrogen at –180 °C. Longer blot time consistently yielded dissociated complexes, pointing to a time-dependent dissociation of the complexes at the air-water interface<sup>39</sup>. The addition of Nb32 significantly enhanced the number of intact complexes (Extended Data Fig. 2).

Data acquisition at the Howard Hughes Medical Institute Janelia Research Campus was done on an FEI Titan Krios (Janelia Krios 1) operating at 300 kV equipped with a spherical aberration corrector, an energy filter (Gatan GIF Quantum), and a post-GIF K2 Summit direct electron detector. Images were obtained in super-resolution counting mode with a super-resolution pixel size of 0.52 Å, which corresponds to a physical pixel size of 1.04 Å. An energy slit with a width of 20 eV was used during data collection. Fully automated data collection was carried out using the SerialEM software<sup>40</sup>. Initial data collection and analysis showed that intact megaplex particles exhibited preferred orientation (Extended Data Fig. 2).

Attempts to alleviate this problem was unsuccessful. Therefore, tilted data collection was employed to improve orientational distribution<sup>41</sup>.

In total, five separate datasets were collected with the stage tilted at 30°, 40°, and 45° on Janelia Krios 1. For an initial dataset comprising 30° and 40° tilted micrographs (Extended Data Fig. 4, dataset 1), the dose rate was set at 8 e<sup>-</sup>/pixel/s and the total exposure time was 14 s, resulting in a total dose of 103.5 e<sup>-</sup>/Å<sup>2</sup>. With dose fractionation set at 0.2 s/frame, each movie series contains 70 frames. For subsequent 40° and 45° tilted data collections (Extended Data Fig. 4, datasets 2–5), the dose rate was set at 8 e<sup>-</sup>/pixel/s and the total exposure time was 14.1 s, resulting in a total dose of 104.3 e<sup>-</sup>/Å<sup>2</sup>. With dose fractionation set at 0.15 s/frame, each movie series contains 94 frames.

All data collected at New York Structural Biology Center (NYSBC) was done on an FEI Titan Krios (NYSBC Krios 2) operating at 300 kV equipped with a spherical aberration corrector, an energy filter (Gatan GIF Quantum), and a post-GIF K2 Summit direct electron detector. Images were obtained in electron counting mode with a physical pixel size of 1.1 Å. An energy slit with a width of 20 eV was used during data collection. Fully automated data collection was carried out using the Leginon software<sup>42</sup>.

In total, two datasets were collected on NYSBC Krios 2. A dataset that comprises 45° and 50° tilted micrographs (Extended Data Fig. 4, dataset 6) had a dose rate of 8.65 e<sup>-</sup>/pixel/s and a total exposure time of 14 s, resulting in a total dose of 103.5 e<sup>-</sup>/Å<sup>2</sup>. With dose fractionation set at 0.2 s/frame, each movie series contains 70 frames. A subsequent dataset of 40° tilted micrographs (Extended Data Fig. 4, dataset 7) was collected with a dose rate of 8.38 e<sup>-</sup>/pixel/s and a total exposure time of 13.95 s, resulting in a total dose of 96.61 e<sup>-</sup>/Å<sup>2</sup>. With dose fractionation set at 0.15 s/frame, each movie series contains 93 frames.

## Data Processing

All data processing operations were performed with Warp v. 1.0.5, Relion 3.0-beta-2, and cryoSPARC v2.4.0 unless otherwise specified<sup>43–45</sup>. Warp was used for gain correction and motion correction of all raw frames, as well as for particle picking and per-particle CTF estimation. Subsequently, particles were extracted for processing in cryoSPARC, where each dataset was first put through 2D classification in order to remove false positives. Multiple rounds of heterogeneous refinement against a megaplex reconstruction and three other decoy structures was performed to clean up the dataset (Extended Data Fig. 3).

Cleaned particles from the NYSBC datasets were rescaled to a pixel size of 1.04Å and combined with particles from the Janelia datasets, resulting in a total of 476,250 megaplex particles. These particles subsequently underwent two rounds of heterogeneous refinement against a megaplex reconstruction and three other decoy structures, resulting in 317,529 particles that made up the megaplex consensus reconstruction (Extended Data Fig. 4, 5). The map was sharpened within cryoSPARC using an estimated b-factor of -202.3 Å<sup>2</sup>.

To obtain a higher resolution reconstruction of the β<sub>2</sub>V<sub>2</sub>R-Gs portion, signal subtraction was performed in Relion to subtract density corresponding to T4L and the Nb32-V<sub>2</sub>T-βarr1-Fab30 portion of the megaplex. The signal subtracted particle stack was further cleaned

through one round of cryoSPARC heterogeneous refinement against a segmented  $\beta_2V_2R$ -Gs map and three decoy structures, resulting in 299,893  $\beta_2V_2R$ -Gs particles. Finally, these particles were refined in cryoSPARC using non-uniform refinement followed by local non-uniform refinement, resulting in a final reconstruction of the  $\beta_2V_2R$ -Gs portion at 3.8Å (Extended Data Figs. 4,6). The map was sharpened within cryoSPARC using an estimated b-factor of  $-133.6 \text{ \AA}^2$ .

As the  $\beta_{arr1-V_2T}$  portion (which contains the Nb32- $V_2T$ - $\beta_{arr1-Fab30}$  portion of the megaplex) is much smaller than the  $\beta_2V_2R$ -Gs portion, we first performed multibody refinement within Relion, subtracted the T4L- $\beta_2V_2R$ -Gs portion from the particle images, and re-centered them on the  $\beta_{arr1-V_2T}$  density. These subtracted, re-centered  $\beta_{arr1-V_2T}$  particles were put through two rounds of cryoSPARC heterogeneous refinement against a segmented Nb32- $V_2T$ - $\beta_{arr1-Fab30}$  map and three decoy structures, resulting in 230,021 particles. Finally, these particles were refined in cryoSPARC using non-uniform refinement, followed by local non-uniform refinement, resulting in a final reconstruction at 4.0Å (Extended Data Figs. 4,6). The map was sharpened within cryoSPARC using an estimated b-factor of  $-139 \text{ \AA}^2$ .

The signal-subtracted reconstructions were fitted within and resampled on the grid of the consensus megaplex reconstruction using the vop resample command within UCSF Chimera.

For each reconstruction, gold-standard fourier shell correlation (FSC = 0.143 criterion) was determined within cryoSPARC, and local resolution was determined using the program MonoRes, implemented within cryoSPARC<sup>45,46</sup>. Three-dimensional FSC (3D-FSC) to assess for directional resolution anisotropy was determined using the 3D-FSC web server (<https://3dfsc.salk.edu>)<sup>41</sup>. To calculate map-to-model sphericity, the models were converted to density maps at 2.08 Å using Chimera. To make the mask, the models were converted to density maps at 8 Å using Chimera and binarized using Relion 3 with a soft Gaussian edge of 3 pixels. The FSC and 3D-FSC of map to model was calculated between the sharpened density maps and the model density map using the 3DFSC server at a FSC threshold of 0.5, after applying the aforementioned mask. Finally, map-to-model FSC (FSC = 0.5 criterion) was determined using phenix.mtriage<sup>47</sup>.

## Model Building

The  $\beta_2V_2R$ -Gs and  $\beta_{arr1-V_2T}$  portions of the megaplex were modeled using the  $\beta_2AR$ -Gs-Nb35 (PDB: 3SN6) and the  $V_2Rpp$ - $\beta_{arr1-Fab30}$  (PDB: 4JQI) crystal structures as starting points, respectively. A homology model of Nb32 was generated using the I-TASSER web server<sup>48</sup>. The crystal structures were first rigidly fitted into their corresponding signal-subtracted maps in UCSF Chimera, followed by manual adjustments and model building in Coot<sup>49,50</sup>. Atomic models for each subcomplexes were refined against the signal-subtracted density map using phenix.real\_space\_refine with Ramachandran, rotamer, torsion, and secondary structure restraints enforced<sup>47</sup>. Additional modeling and manual adjustments were performed in Coot and the modeling statistics were validated using MolProbity<sup>51</sup>. All structural comparisons and figures were made with UCSF Chimera, UCSF ChimeraX, and PyMOL ([pymol.org](http://pymol.org))<sup>49,52</sup>.

### Coarse-grained Molecular Dynamics (MD) Simulations

All MD starting structures were modified from the cryo-EM structure to allow for proper receptor placement in a DPPC membrane. The linker (343-ARGGRTPPSLGPQD-355) from the end of helix 8 to the C terminal tail of the receptor was modeled in through PyMOL ([pymol.org](http://pymol.org)) and clashes between side chains were minimized using PyMOL sculpting tool. These structures was then embedded in a 30 nm DPPC lipid bilayer and set up for martini coarse graining using the CHARMM\_GUI website<sup>53,54</sup>. All MD calculations were performed using the SBgrid software package with GROMACS 2018.1 at 303K<sup>55</sup>. The complex was minimized in 10,000 steps and subjected to 5 rounds of equilibration, each of 1 ns, to stabilize the system with a time interval of 0.02 ps between calculations. 30 nanoseconds of production were run on each MD to ensure stability of the complex. All final MD structures were visualized and analyzed through VMD and PyMOL<sup>56</sup>.

### Liquid Chromatography-Tandem Mass Spectrometry (LC-MS/MS)

All solvents are of MS-grade and purchased from Fisher Scientific, unless otherwise specified. Gel-bands were cut into small pieces of approximately 1mm<sup>3</sup> using a scalpel and destained, reduced and alkylated as previously described<sup>57</sup>. Digestion was carried out at 37°C overnight using a combination of sequencing grade trypsin (Promega) and endopeptidase LysC (Wako Chemicals). Two iterations of peptide extraction were performed using 70% acetonitrile, 5% formic acid in water and peptides were dried using a vacuum centrifuge (Savant).

Liquid chromatography was performed on a Dionex 3000 Ultimate HPLC equipped with a NCS3500RS nano- and microflow pump (Dionex). Peptides were loaded onto a 100 µm\*20mm Acclaim PepMap C18 trap column (Thermo Scientific) at 3µL/min. Solvent A consisted of 0.1 % formic acid in water and solvent B consisted of 0.1% formic acid, 80% acetonitrile in water. Separation was achieved using a 75µm\*120mm pulled-emitter nanocolumn (Nikkyo Technos). Solvent B went from 1% – 38% over 70 minutes followed by a sharp 1-minute increase to 90% where it was kept for 13 minutes. Peptides were analyzed using a Q-Exactive HF mass spectrometer (Thermo Scientific) operating in positive ion mode. For the data-dependent analyses, spectra were recorded in data dependent acquisition (DDA) mode, selecting the 20 most abundant ions for fragmentation within each duty cycle. MS1 resolution was set to 60 000 and an MS2 resolution was set to 30 000. AGC targets of 3e6 (MS1) and 2e5 (MS2) were applied.

A parallel reaction monitoring (PRM) method was designed to target two peptides from the C-terminus which were found to be phosphorylated from the DDA experiment. The targets were TPPSLGPQDESCCTASSSLAK with 0–3 phosphorylations and GRTPPSLGPQDESCCTASSSLAK with 0–4 phosphorylations.

Data was searched using MaxQuant v. 1.6.2<sup>58</sup>. Default settings were applied. Phosphorylation of S and T and oxidation of M were applied as variable modifications. Carbamidomethylation of C was applied as a static modification. A maximum of 8 possible modifications per peptide was allowed. Match between runs was enabled. Collapsed

phosphosite information was exported, from which the localization probabilities for phosphorylations at individual residues could be determined<sup>59</sup>.

MS1 peak areas were extracted using Skyline v. 4.1.0.18169<sup>60</sup>. Peak areas from the two peptide targets were collapsed to provide an intensity for the region of interest with varying number phosphorylations. Intensity values of the C-terminal region were normalized based on all identified peptides from the protein.

The mass spectrometry proteomics data have been deposited to the ProteomeXchange Consortium via the PRIDE partner repository with the dataset identifier PXD015298.

### Real-time cAMP measurement

Previously described  $\beta$ arr1/ $\beta$ arr2/ $\beta_2$ AR triple-knockout HEK293 cells were transiently co-transfected with plasmids encoding the bioluminescence resonance energy transfer (BRET)-based CAMYEL cAMP biosensor (YFP-Epac-Rluc) and either  $\beta_2$ V<sub>2</sub>R,  $\beta_2$ V<sub>2</sub>R- $\beta$ arr1,  $\beta_2$ V<sub>2</sub>R- $\beta$ arr1, or pcDNA3.1(+) mock control<sup>11</sup>. Twenty-four hours after transfection, the cells were plated in poly-D-lysine coated white 96-well plates (Corning, USA) and incubated overnight. Forty-eight hours after transfection, the cells were washed and placed in assay buffer (HBSS + 10 mM HEPES, pH 7.4) at 37 °C for 30 min. Cells were loaded with 5  $\mu$ M luciferase substrate coelenterazine H for 5 min and BRET was detected through Rluc8 luminescence (480 nm) and YFP fluorescence (530 nm) measurements using a CLARIOstar Plus plate reader (BMG Labtech). After a 2-min basal period, cells were challenged with 1  $\mu$ M BI-167107. Forskolin (10  $\mu$ M) was used as a positive control, and regular assay buffer as a negative/baseline control. All data was subsequently normalized to the 10  $\mu$ M Forskolin control. Data represents mean  $\pm$  S.E.M. of four independent experiments for the  $\beta_2$ V<sub>2</sub>R- $\beta$ arr1 and  $\beta_2$ V<sub>2</sub>R- $\beta$ arr2 conditions and of three independent experiments for the  $\beta_2$ V<sub>2</sub>R condition. Ordinary one-way ANOVA with Holm-Sidak's multiple comparison post-hoc test was performed to determine statistical significance between mock control and the  $\beta_2$ V<sub>2</sub>R or  $\beta_2$ V<sub>2</sub>R- $\beta$ arr1/2 conditions.

Further information on experimental design is available in the Nature Research Reporting Summary linked to this article.

### Data Availability

Cryo-EM maps corresponding to the consensus megaplex reconstruction as well as the signal-subtracted  $\beta_2$ V<sub>2</sub>R-Gs and  $\beta$ arr1-V<sub>2</sub>T subcomplexes have been deposited in the Electron Microscopy Data Bank (EMDB) with accession codes EMD-9377, EMD-9376, and EMD-9375, respectively. Atomic coordinates for the  $\beta_2$ V<sub>2</sub>R-Gs and  $\beta$ arr1-V<sub>2</sub>T subcomplexes have been deposited in the Protein Data Bank (PDB) with accession codes PDB-6NI3 and PDB-6NI2, respectively. The mass spectrometry proteomics data have been deposited to the ProteomeXchange Consortium via the PRIDE partner repository with the dataset identifier PXD015298. Source data for Extended Data Figures 1c and 1d are available with the paper online. Other data that support the findings of this study are available from the corresponding authors upon request.

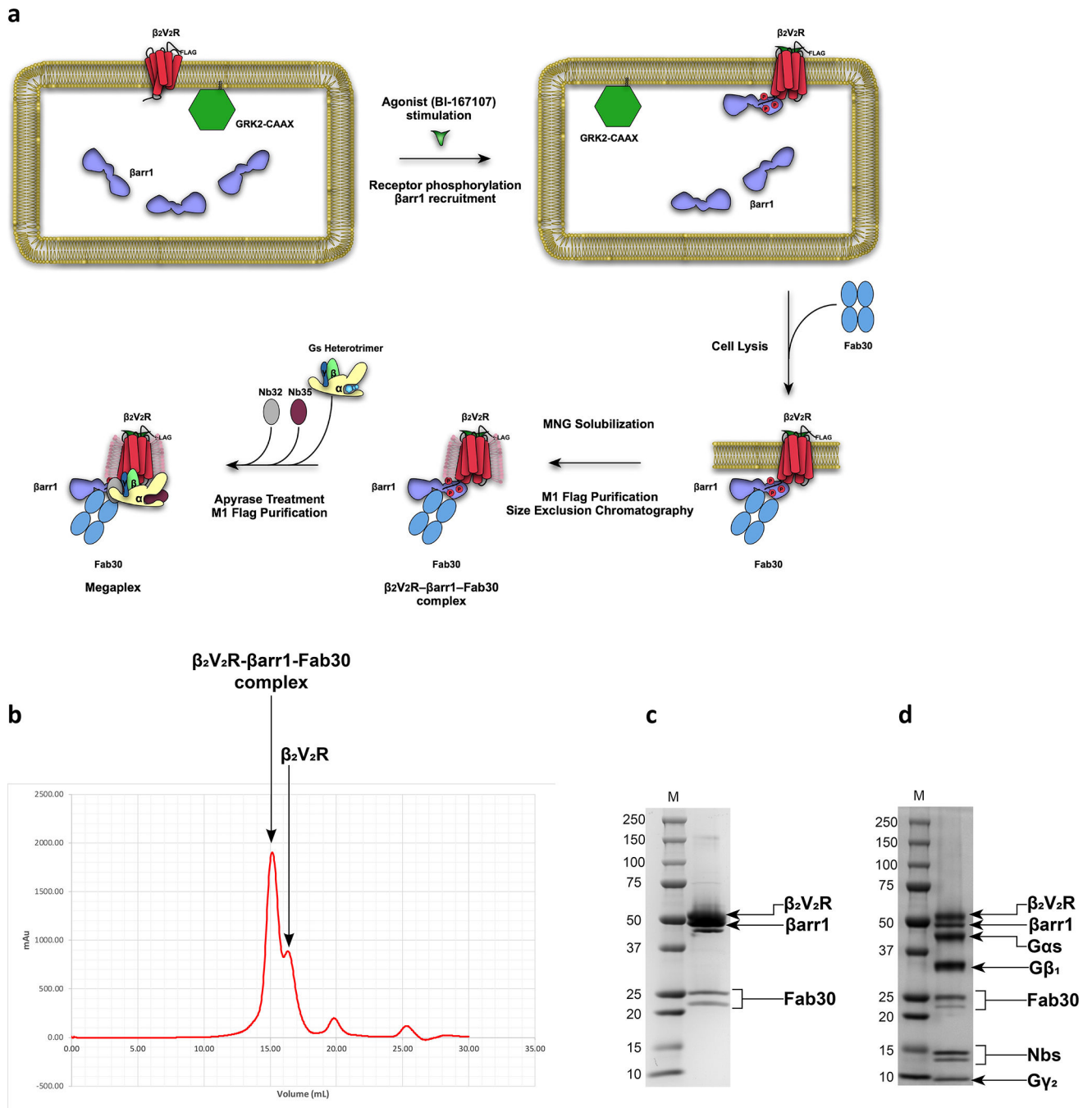
## Extended Data

Author Manuscript

Author Manuscript

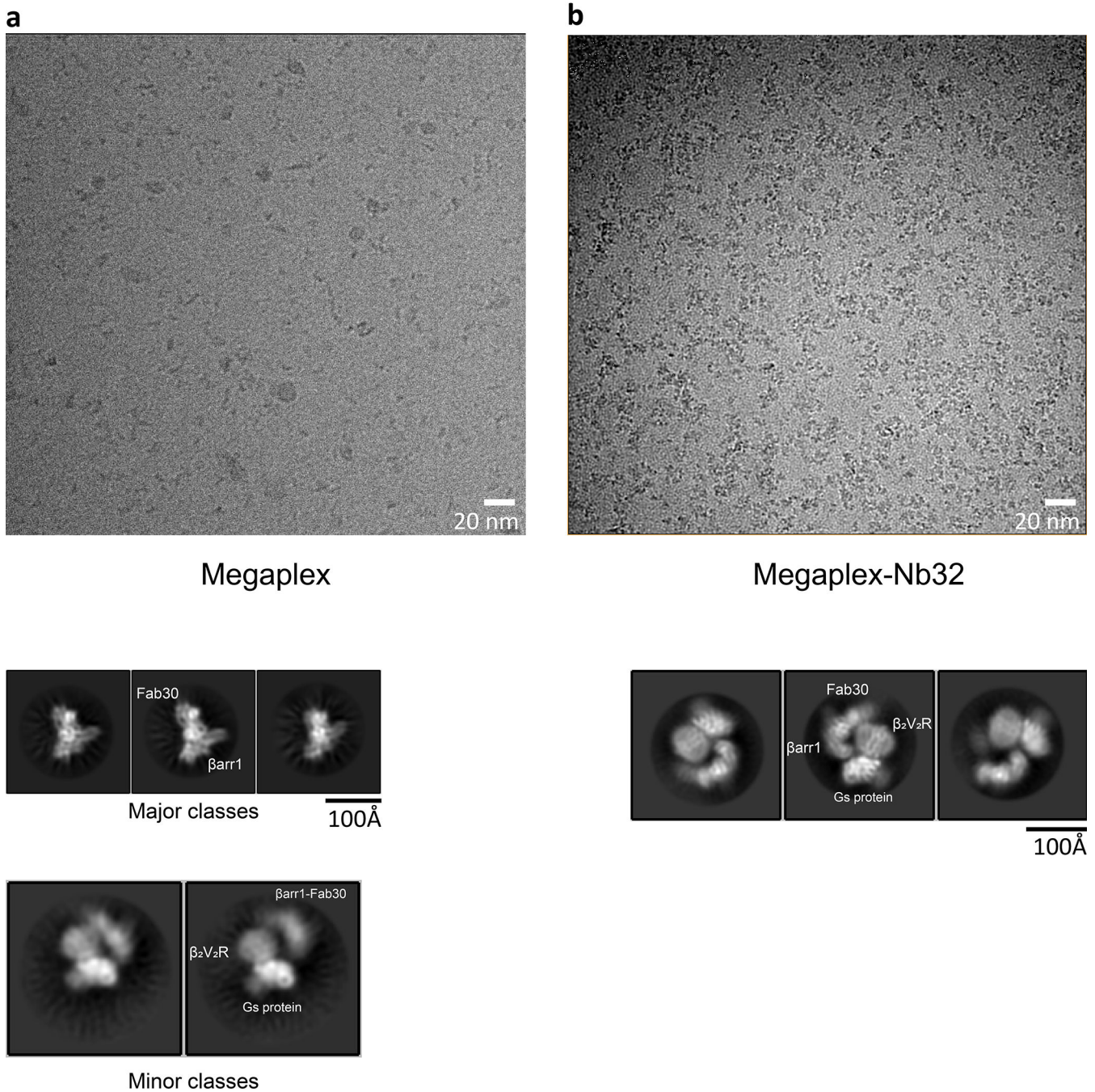
Author Manuscript

Author Manuscript



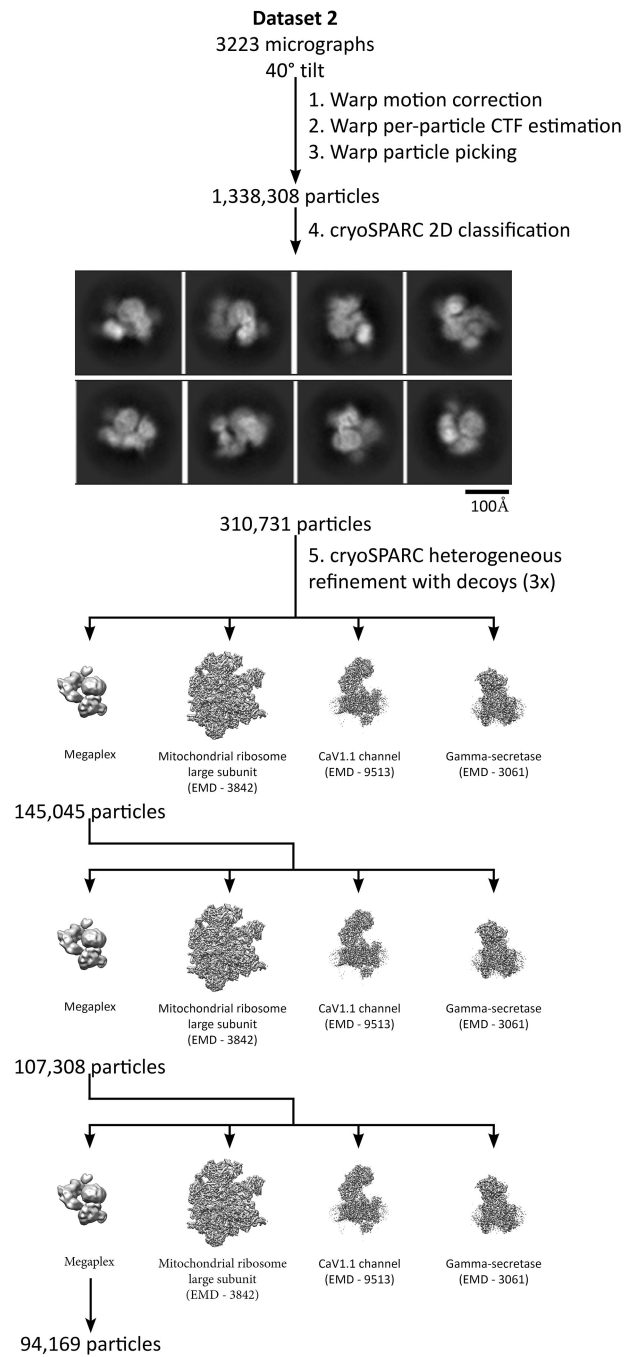
**Extended Data Fig. 1: Sample preparation and purification of the megaplex.**

**a**, Schematic illustration of the purification and *in vitro* formation procedure of the megaplex. **b**, Size exclusion chromatogram of the precursor β<sub>2</sub>V<sub>2</sub>R-βarr1-Fab30 complex. **c**, SDS-PAGE gel of the β<sub>2</sub>V<sub>2</sub>R-βarr1-Fab30 complex after purification by size exclusion chromatography. **d**, SDS-PAGE gel of the megaplex after *in vitro* formation and M1 anti-Flag purification. For **c-d**, M denotes molecular weight (kDa) marker. Uncropped gel images for Extended Data Fig. 1c,d are provided as Source Data.



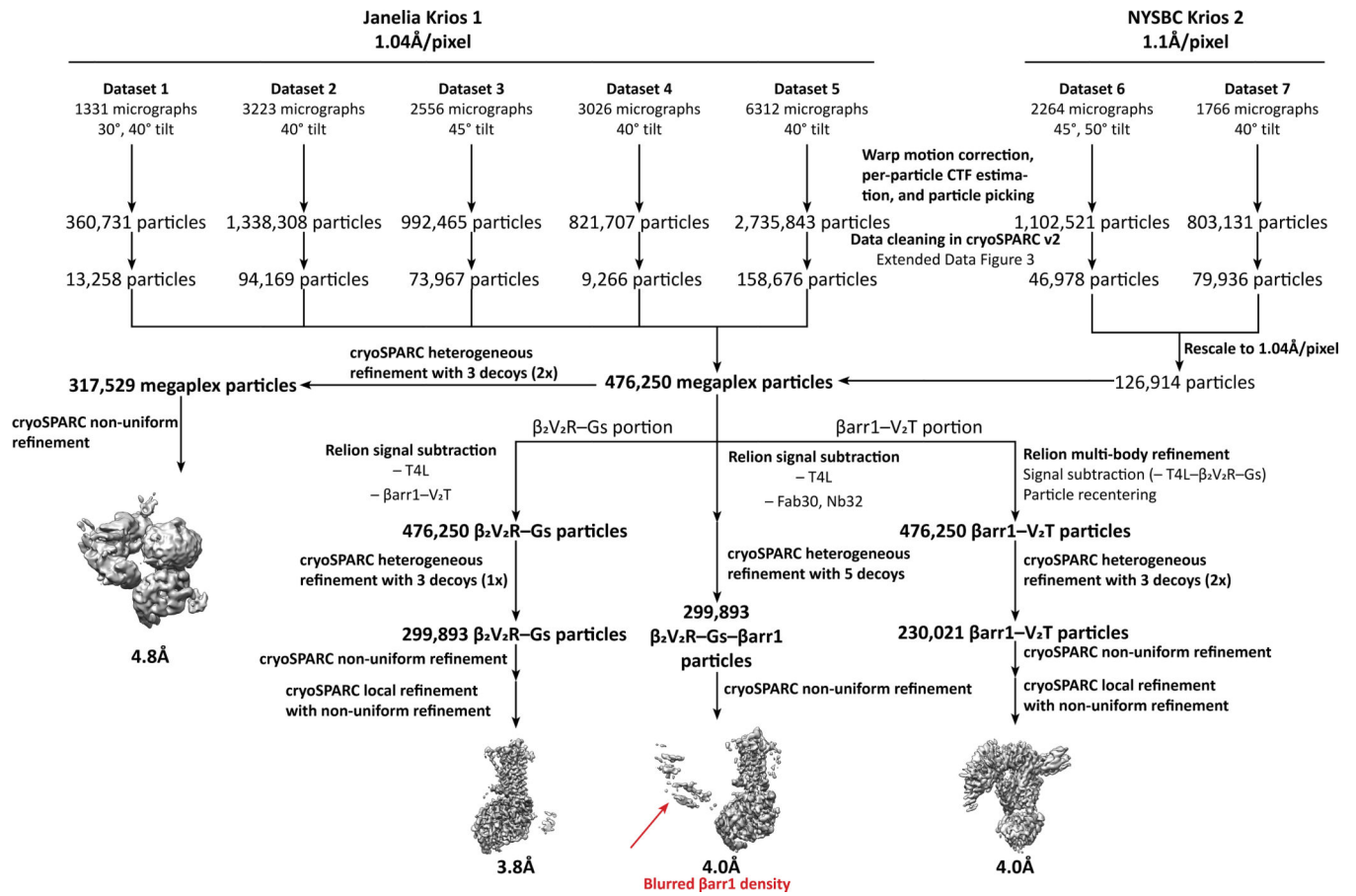
**Extended Data Fig. 2: Nanobody 32 (Nb32) stabilizes the megaplex.**

**a**, Representative micrograph and 2D class averages of megaplex samples prepared without nanobody 32 (Nb32), displaying a small percentage of megaplexes. **b**, Same as in **a**, but with a megaplex sample prepared with Nb32.

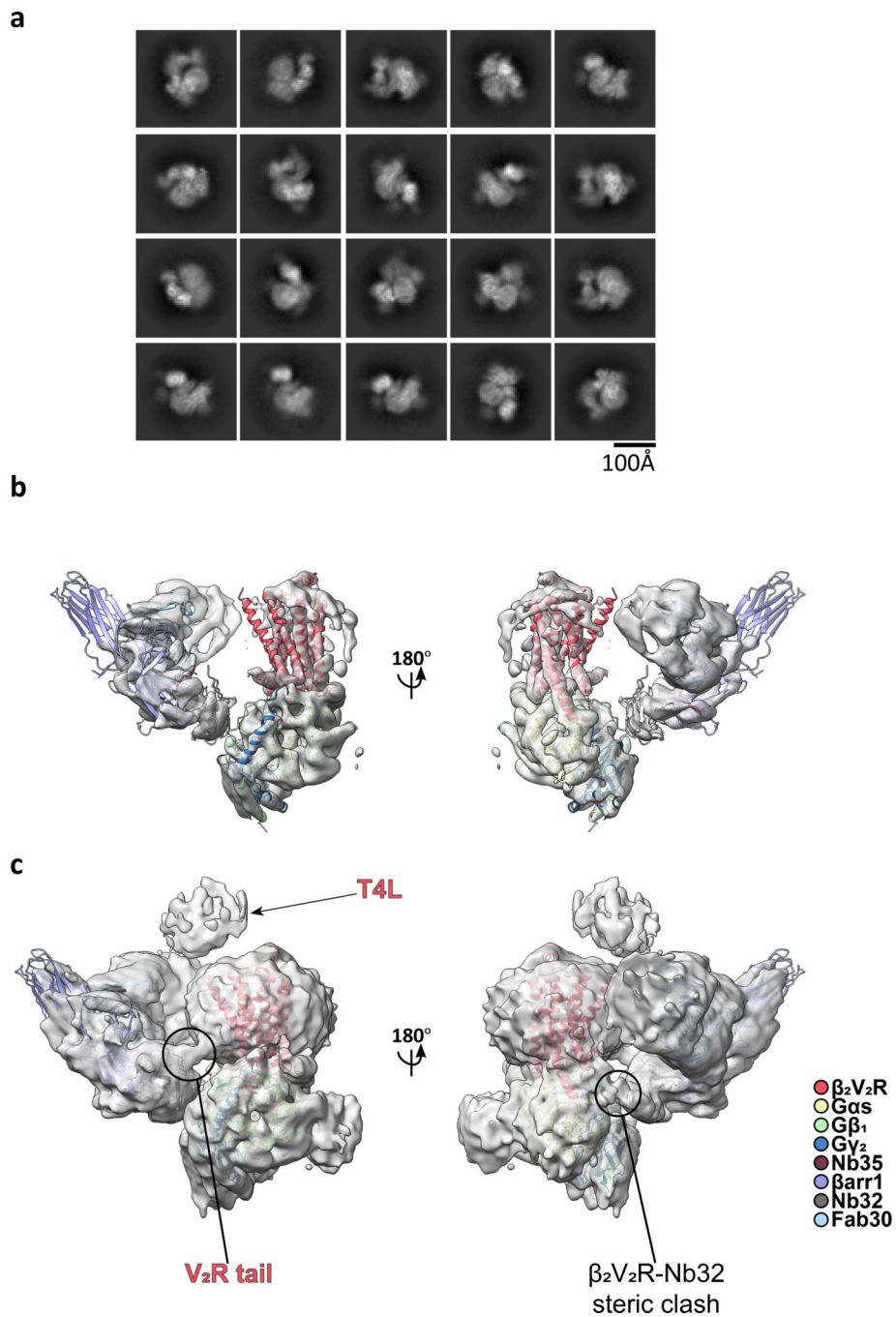


**Extended Data Fig. 3: A procedure utilizing Warp and cryoSPARC for initial data processing and cleaning of one representative dataset (Dataset 2).**

The same procedure was used on all dataset.

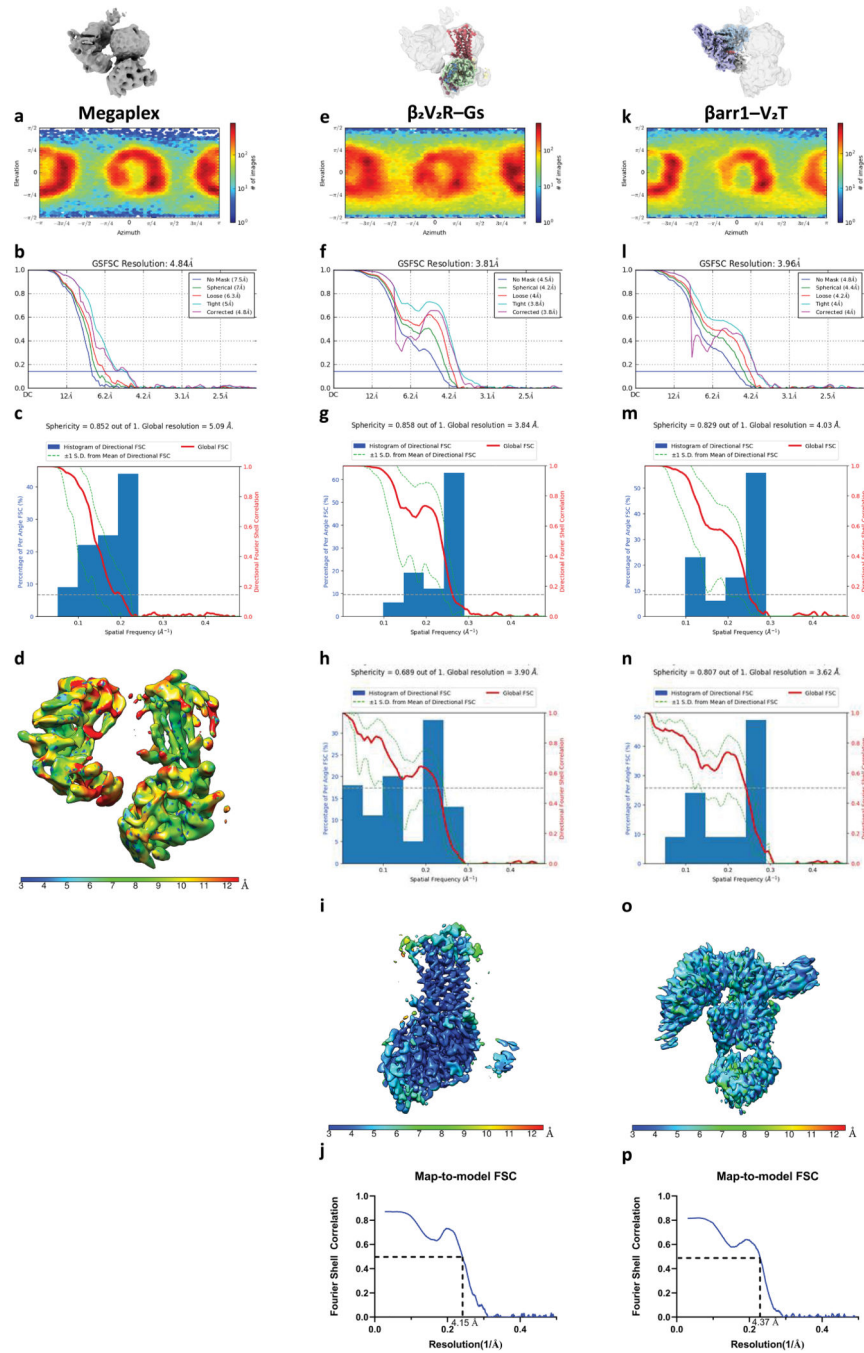


**Extended Data Fig. 4:**  
Data processing workflow for all datasets of the megaplex.

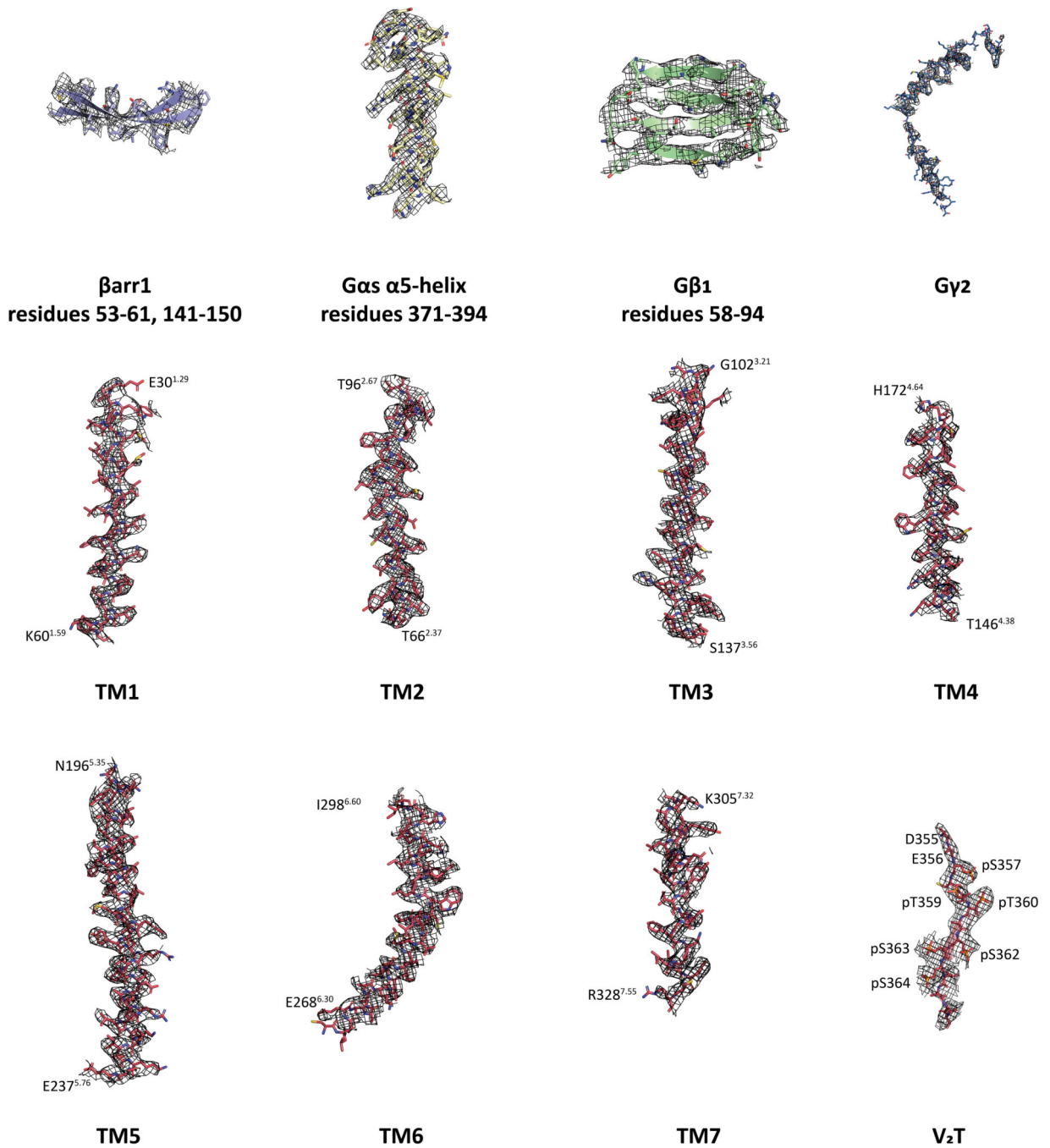


**Extended Data Fig. 5: Megaplex consensus reconstruction.**

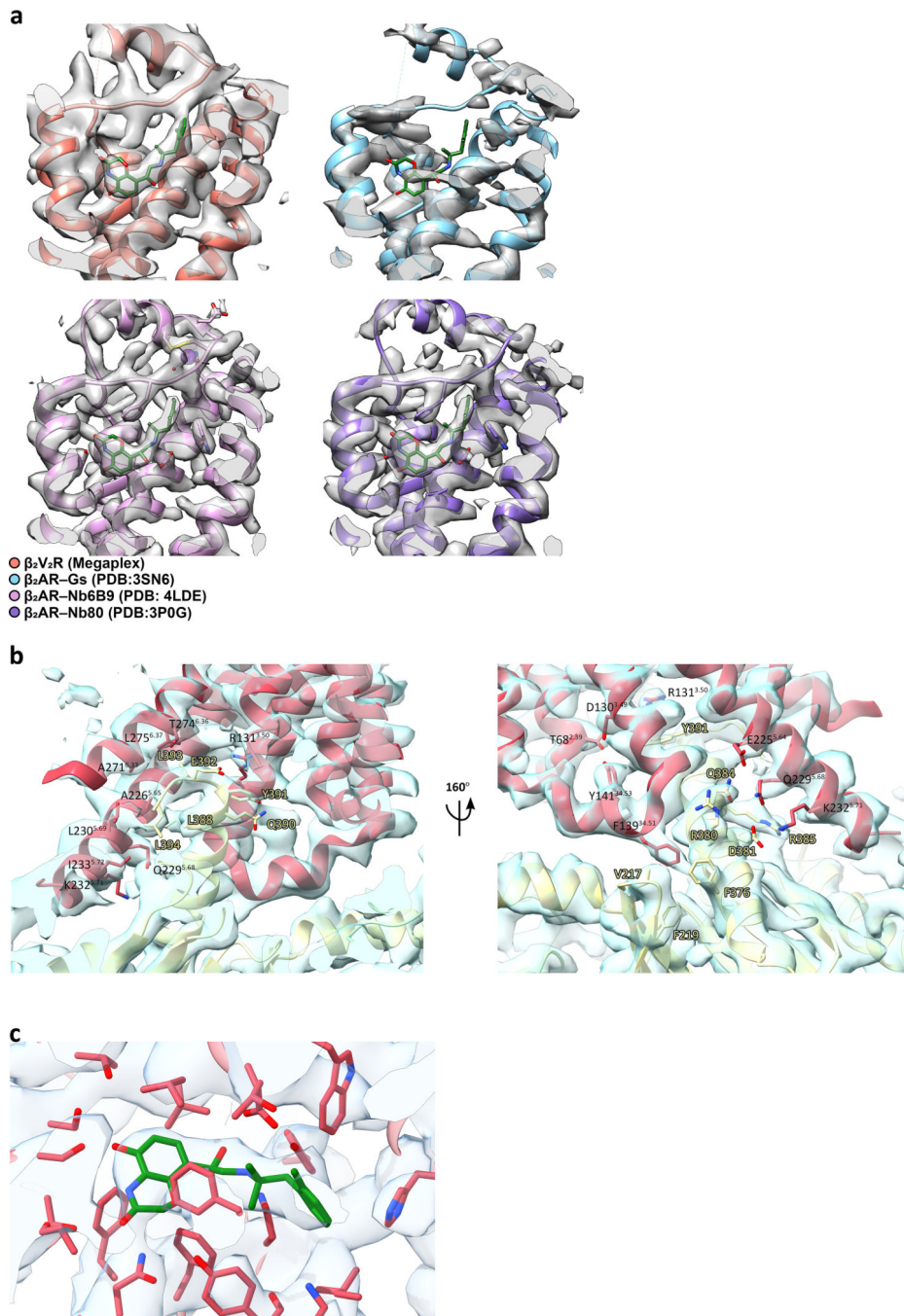
**a**, Representative 2D class averages of the consensus megaplex reconstruction. **b-c**, The megaplex reconstruction is shown at high (0.115) threshold (**b**), and low (0.05) threshold (**c**). The T4L and flexible portion of the V<sub>2</sub>T appears at a lower threshold. The atomic models of the components, derived from signal subtracted reconstructions, are fitted to the consensus reconstruction. Densities for the flexible V<sub>2</sub>T and steric clash between the β<sub>2</sub>V<sub>2</sub>R and Nb32 are denoted by black circles.



**Extended Data Fig. 6: Orientational distribution and resolution measurements of the megaplex. a-d**, orientational distribution (a), FSC curves indicating overall resolution (FSC = 0.143) (b), 3D-FSC to assess directional resolution anisotropy (c), and local resolution measurements (d) of the megaplex consensus reconstruction. **e-j**, orientational distribution (e), FSC curves indicating overall resolution (FSC = 0.143) (f), 3D-FSC to assess directional resolution anisotropy (g), map-to-model FSC and sphericity (h), local resolution measurements (i), and map-to-model FSC curve (j) of the  $\beta_2V_2R$ -Gs reconstruction. **k-p**, same as **e-j**, but for the  $\beta arr1$ -V<sub>2</sub>T reconstruction.

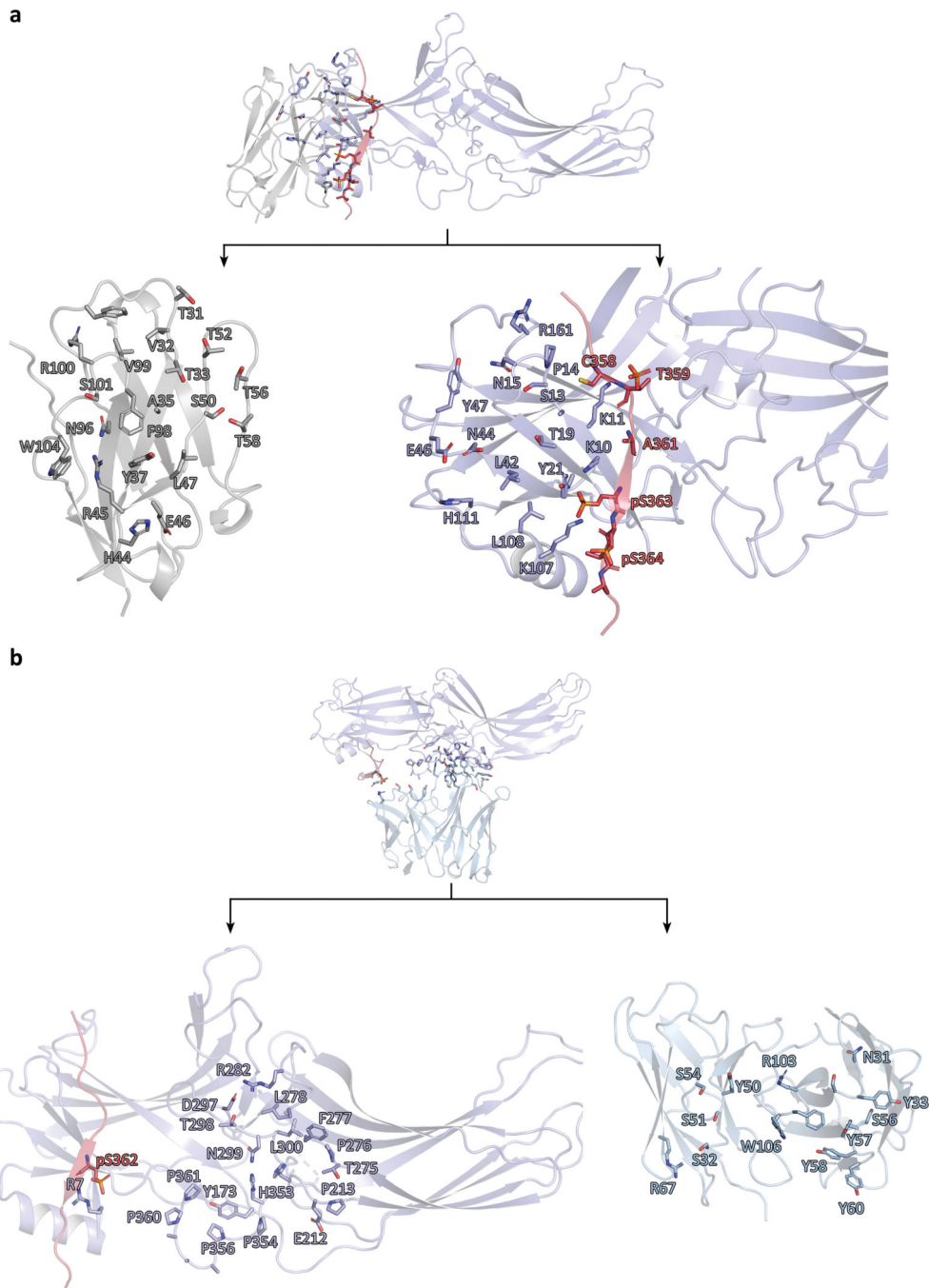


**Extended Data Fig. 7: Representative densities in black mesh of various protein components.** Representative densities, from the 3.8Å β<sub>2</sub>V<sub>2</sub>R–Gs and 4.0Å βarr1–V<sub>2</sub>T structures, of the β<sub>2</sub>V<sub>2</sub>R, Gs subunits, and βarr1.



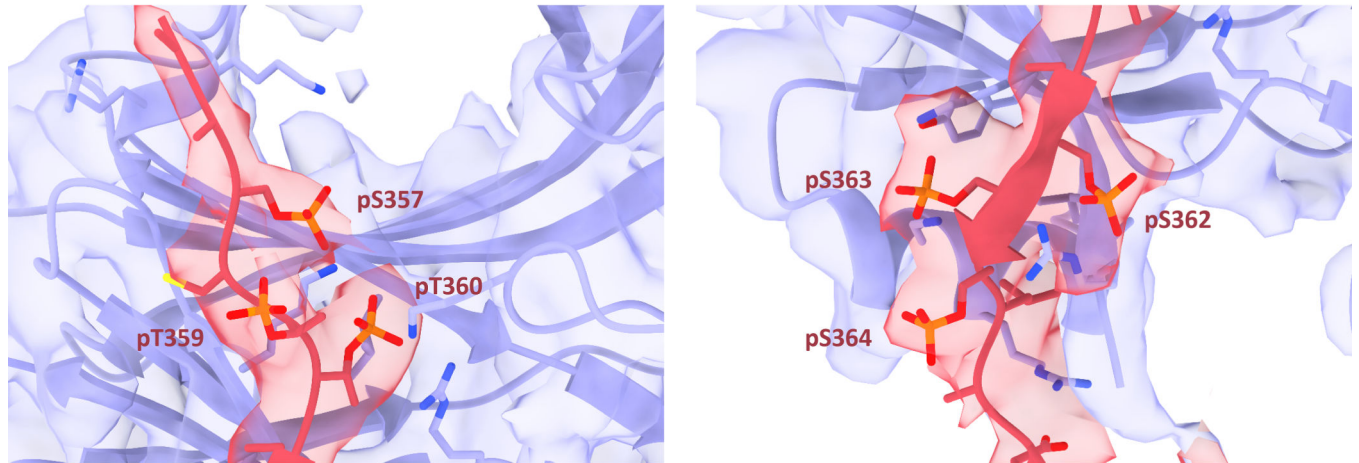
**Extended Data Fig. 8: Representative density of the  $\beta_2$ V<sub>2</sub>R-Gs portion of the megaplex, and comparison against other active  $\beta_2$ AR structures.**

**a**, Comparison of the binding pose of BI-167107 (BI) in the megaplex against three other available BI-bound  $\beta_2$ AR structures. BI is colored green. **b**, Representative density showing contacts between the  $\beta_2$ V<sub>2</sub>R and Gs in the megaplex. **c**, The BI binding pocket within the megaplex, accompanied by EM density for all residues within 5 Å of the ligand.



**Extended Data Fig. 9: Interaction between Fab30, V<sub>2</sub>T and protein stabilizers.**  
**a-b,** Interface between  $\beta$ arr1 and V<sub>2</sub>T with either Nb32 (**a**) or Fab30 (**b**). Interface residues are labeled.

**a**



**b**

<sup>347</sup>**T**PP**S**LG**P**QDE**S**CT**T**ASS**S**LAK<sup>367</sup>

Residues	Localization Probability (Unstimulated $\beta_2V_2R$ )	Localization Probability (Stimulated $\beta_2V_2R$ )
<b>T347</b>	1	1
<b>S350</b>	1	1
<b>S357</b>	0	0.87
<b>T359</b>	0	0.97
<b>T360</b>	0	0.84
<b>S362</b>	0	0.97
<b>S363</b>	0.85	0.91
<b>S364</b>	0.84	0.99

**Extended Data Fig. 10: Verification of observed phosphorylation sites on the  $V_2T$ .**

**a**, Cryo-EM density for the six phosphorylated residues on the  $V_2T$ . **b**, Localization probabilities of eight potential sites of phosphorylation on the  $V_2T$  assessed by LC-MS/MS. A trypsin-digested fragment of the  $V_2T$  is displayed. Bolded residues are phosphorylation sites observed in the cryo-EM map. Residues in red were not observed in the map, and yellow-highlighted residues were phosphorylated in both unstimulated and BI-stimulated receptors.

### Supplementary Material

Refer to Web version on PubMed Central for supplementary material.

## Acknowledgments

We thank Q. Lennon, J. Bisson and J. Taylor for excellent administrative support, W. Capel for technical support, Y. Zhang and G. Skiniotis for help with initial sample screening, C.-R. Liang, L.-L. Gu and J.-M. Shan for synthesizing BI-167107, T. Wang and the CUNY Advanced Science Research Center Imaging Facility for help with sample screening and data collection, the lab of K. Gardner at the CUNY Advanced Science Research Center for providing various general lab reagents and equipment during initial sample screening, M. Walters, M. DeLong, M. Plue, T. Milledge, D. Capel and X. Jiang at Duke University for technical support and discussion, D. Lyumkis, D. Tegunov, W. Rice, E. Eng, L. Kim, M. Kopylov and A. Cheng for help with tilted data collection and processing and S. Houston and B. Plouffe for helpful discussion.

This work received support from NIH grants (nos. T32GM007171 and F30HL149213 to A.H.N.; F30HL129803 to T.J.C.; T32GM007767 to J.P.M.; R35GM133598 to A.d.G. and R01HL016037 to R.J.L.); HHMI Medical Research Fellowship to A.H.N.; the Danish Council for Independent Research & Lundbeck Foundation (DFE-5053-00136 and R172-2014-1468 to A.R.B.T.); American Heart Association Innovative Project Award (no. 19IPLOI34760706 to A.d.G.); Institut de Recherche Servier (no. 18021932 to A.d.G. and D.B.-H.); and American Heart Association Predoctoral Fellowship (no. 13PRE17110027 to J.P.M.). Some of this work was performed at the Simons Electron Microscopy Center and National Resource for Automated Molecular Microscopy located at the New York Structural Biology Center, supported by grants from the Simons Foundation (grant no. SF349247), NYSTAR, and the NIH National Institute of General Medical Sciences (grant no. GM103310) with additional support from Agouron Institute (grant no. F00316) and the NIH (grant no. OD019994). R.J.L. is an HHMI Investigator.

## References

1. Reiter E, Ahn S, Shukla AK & Lefkowitz RJ Molecular mechanism of beta-arrestin-biased agonism at seven-transmembrane receptors. *Annu Rev Pharmacol Toxicol* 52, 179–97 (2012). [PubMed: 21942629]
2. Lefkowitz RJ, Stadel JM & Caron MG Adenylate cyclase-coupled beta-adrenergic receptors: structure and mechanisms of activation and desensitization. *Annu Rev Biochem* 52, 159–86 (1983). [PubMed: 6137187]
3. Rajagopal S, Rajagopal K & Lefkowitz RJ Teaching old receptors new tricks: biasing seven-transmembrane receptors. *Nat Rev Drug Discov* 9, 373–86 (2010). [PubMed: 20431569]
4. Oakley RH, Laporte SA, Holt JA, Barak LS & Caron MG Association of beta-arrestin with G protein-coupled receptors during clathrin-mediated endocytosis dictates the profile of receptor resensitization. *Journal of Biological Chemistry* 274, 32248–32257 (1999). [PubMed: 10542263]
5. Oakley RH, Laporte SA, Holt JA, Caron MG & Barak LS Differential affinities of visual arrestin, beta arrestin1, and beta arrestin2 for G protein-coupled receptors delineate two major classes of receptors. *J Biol Chem* 275, 17201–10 (2000). [PubMed: 10748214]
6. Calebiro D et al. Persistent cAMP-signals triggered by internalized G-protein-coupled receptors. *PLoS Biol* 7, e1000172 (2009). [PubMed: 19688034]
7. Ferrandon S et al. Sustained cyclic AMP production by parathyroid hormone receptor endocytosis. *Nat Chem Biol* 5, 734–42 (2009). [PubMed: 19701185]
8. Feinstein TN et al. Noncanonical control of vasopressin receptor type 2 signaling by retromer and arrestin. *J Biol Chem* 288, 27849–60 (2013). [PubMed: 23935101]
9. Thomsen ARB et al. GPCR-G Protein-beta-Arrestin Super-Complex Mediates Sustained G Protein Signaling. *Cell* 166, 907–919 (2016). [PubMed: 27499021]
10. Shukla AK et al. Visualization of arrestin recruitment by a G-protein-coupled receptor. *Nature* 512, 218–222 (2014). [PubMed: 25043026]
11. Cahill TJ 3rd et al. Distinct conformations of GPCR-beta-arrestin complexes mediate desensitization, signaling, and endocytosis. *Proc Natl Acad Sci U S A* 114, 2562–2567 (2017). [PubMed: 28223524]
12. Wehbi VL et al. Noncanonical GPCR signaling arising from a PTH receptor-arrestin-Gbetagamma complex. *Proc Natl Acad Sci U S A* 110, 1530–5 (2013). [PubMed: 23297229]
13. Jimenez-Vargas NN et al. Protease-activated receptor-2 in endosomes signals persistent pain of irritable bowel syndrome. *Proc Natl Acad Sci U S A* 115, E7438–E7447 (2018). [PubMed: 30012612]

14. Wanka L, Babilon S, Kaiser A, Morl K & Beck-Sickinger AG Different mode of arrestin-3 binding at the human Y1 and Y2 receptor. *Cell Signal* 50, 58–71 (2018). [PubMed: 29944985]
15. Rasmussen SG et al. Crystal structure of the beta2 adrenergic receptor-Gs protein complex. *Nature* 477, 549–55 (2011). [PubMed: 21772288]
16. Cherezov V et al. High-resolution crystal structure of an engineered human beta2-adrenergic G protein-coupled receptor. *Science* 318, 1258–65 (2007). [PubMed: 17962520]
17. Ballesteros JA, Weinstein. H Integrated methods for the construction of three-dimensional models and computational probing of structure-function relations in G protein-coupled receptors. *Methods in Neurosciences*, 366–428 (1995).
18. Ring AM et al. Adrenaline-activated structure of beta2-adrenoceptor stabilized by an engineered nanobody. *Nature* 502, 575–579 (2013). [PubMed: 24056936]
19. Rasmussen SG et al. Structure of a nanobody-stabilized active state of the beta(2) adrenoceptor. *Nature* 469, 175–80 (2011). [PubMed: 21228869]
20. Shukla AK et al. Structure of active beta-arrestin-1 bound to a G-protein-coupled receptor phosphopeptide. *Nature* 497, 137–41 (2013). [PubMed: 23604254]
21. Fredericks ZL, Pitcher JA & Lefkowitz RJ Identification of the G protein-coupled receptor kinase phosphorylation sites in the human beta2-adrenergic receptor. *J Biol Chem* 271, 13796–803 (1996). [PubMed: 8662852]
22. Lally CC, Bauer B, Selent J & Sommer ME C-edge loops of arrestin function as a membrane anchor. *Nat Commun* 8, 14258 (2017). [PubMed: 28220785]
23. Zhou XE et al. Identification of Phosphorylation Codes for Arrestin Recruitment by G Protein-Coupled Receptors. *Cell* 170, 457–469 e13 (2017). [PubMed: 28753425]
24. Lohse MJ, Benovic JL, Codina J, Caron MG & Lefkowitz RJ beta-Arrestin: a protein that regulates beta-adrenergic receptor function. *Science* 248, 1547–50 (1990). [PubMed: 2163110]
25. Lohse MJ et al. Receptor-specific desensitization with purified proteins. Kinase dependence and receptor specificity of beta-arrestin and arrestin in the beta 2-adrenergic receptor and rhodopsin systems. *J Biol Chem* 267, 8558–64 (1992). [PubMed: 1349018]
26. Kang Y et al. Crystal structure of rhodopsin bound to arrestin by femtosecond X-ray laser. *Nature* 523, 561–7 (2015). [PubMed: 26200343]
27. Liang YL et al. Phase-plate cryo-EM structure of a class B GPCR-G-protein complex. *Nature* 546, 118–123 (2017). [PubMed: 28437792]
28. Zhang Y et al. Cryo-EM structure of the activated GLP-1 receptor in complex with a G protein. *Nature* 546, 248–253 (2017). [PubMed: 28538729]
29. Le Gouill C, Innamorati G & Birnbaumer M An expanded V2 receptor retention signal. *FEBS Lett* 532, 363–6 (2002). [PubMed: 12482593]
30. Innamorati G, Sadeghi HM, Tran NT & Birnbaumer M A serine cluster prevents recycling of the V2 vasopressin receptor. *Proc Natl Acad Sci U S A* 95, 2222–6 (1998). [PubMed: 9482866]
31. Mayer D et al. Distinct G protein-coupled receptor phosphorylation motifs modulate arrestin affinity and activation and global conformation. *Nat Commun* 10, 1261 (2019). [PubMed: 30890705]
32. Liang YL et al. Cryo-EM structure of the active, Gs-protein complexed, human CGRP receptor. *Nature* 561, 492–497 (2018). [PubMed: 30209400]
33. Liang YL et al. Phase-plate cryo-EM structure of a biased agonist-bound human GLP-1 receptor-Gs complex. *Nature* 555, 121–125 (2018). [PubMed: 29466332]
34. Irannejad R et al. Conformational biosensors reveal GPCR signalling from endosomes. *Nature* 495, 534–8 (2013). [PubMed: 23515162]
35. Yang M, He RL, Benovic JL & Ye RD beta-Arrestin1 interacts with the G-protein subunits beta1gamma2 and promotes beta1gamma2-dependent Akt signalling for NF-kappaB activation. *Biochem J* 417, 287–96 (2009). [PubMed: 18729826]
36. Gaudet R, Bohm A & Sigler PB Crystal structure at 2.4 angstroms resolution of the complex of transducin betagamma and its regulator, phosducin. *Cell* 87, 577–88 (1996). [PubMed: 8898209]

37. Lodowski DT, Pitcher JA, Capel WD, Lefkowitz RJ & Tesmer JJ Keeping G proteins at bay: a complex between G protein-coupled receptor kinase 2 and Gbetagamma. *Science* 300, 1256–62 (2003). [PubMed: 12764189]
38. Whorton MR & MacKinnon R X-ray structure of the mammalian GIRK2-beta-gamma G-protein complex. *Nature* 498, 190–7 (2013). [PubMed: 23739333]

## Methods-only References

39. Noble AJ et al. Routine single particle CryoEM sample and grid characterization by tomography. *Elife* 7(2018).
40. Mastronarde DN Automated electron microscope tomography using robust prediction of specimen movements. *J Struct Biol* 152, 36–51 (2005). [PubMed: 16182563]
41. Tan YZ et al. Addressing preferred specimen orientation in single-particle cryo-EM through tilting. *Nat Methods* 14, 793–796 (2017). [PubMed: 28671674]
42. Suloway C et al. Automated molecular microscopy: the new Legion system. *J Struct Biol* 151, 41–60 (2005). [PubMed: 15890530]
43. Tegunov D & Cramer P Real-time cryo-EM data pre-processing with Warp. *BioRxiv* (2018).
44. Zivanov J et al. New tools for automated high-resolution cryo-EM structure determination in RELION-3. *Elife* 7(2018).
45. Punjani A, Rubinstein JL, Fleet DJ & Brubaker MA cryoSPARC: algorithms for rapid unsupervised cryo-EM structure determination. *Nat Methods* 14, 290–296 (2017). [PubMed: 28165473]
46. Vilas JL et al. MonoRes: Automatic and Accurate Estimation of Local Resolution for Electron Microscopy Maps. *Structure* 26, 337–344 e4 (2018). [PubMed: 29395788]
47. Adams PD et al. PHENIX: a comprehensive Python-based system for macromolecular structure solution. *Acta Crystallogr D Biol Crystallogr* 66, 213–21 (2010). [PubMed: 20124702]
48. Roy A, Kucukural A & Zhang Y I-TASSER: a unified platform for automated protein structure and function prediction. *Nat Protoc* 5, 725–38 (2010). [PubMed: 20360767]
49. Pettersen EF et al. UCSF Chimera--a visualization system for exploratory research and analysis. *J Comput Chem* 25, 1605–12 (2004). [PubMed: 15264254]
50. Emsley P, Lohkamp B, Scott WG & Cowtan K Features and development of Coot. *Acta Crystallogr D Biol Crystallogr* 66, 486–501 (2010). [PubMed: 20383002]
51. Chen VB et al. MolProbity: all-atom structure validation for macromolecular crystallography. *Acta Crystallogr D Biol Crystallogr* 66, 12–21 (2010). [PubMed: 20057044]
52. Goddard TD et al. UCSF ChimeraX: Meeting modern challenges in visualization and analysis. *Protein Sci* 27, 14–25 (2018). [PubMed: 28710774]
53. Marrink SJ & Mark AE Molecular view of hexagonal phase formation in phospholipid membranes. *Biophys J* 87, 3894–900 (2004). [PubMed: 15377528]
54. Jo S, Kim T, Iyer VG & Im W CHARMM-GUI: a web-based graphical user interface for CHARMM. *J Comput Chem* 29, 1859–65 (2008). [PubMed: 18351591]
55. Pronk S et al. GROMACS 4.5: a high-throughput and highly parallel open source molecular simulation toolkit. *Bioinformatics* 29, 845–54 (2013). [PubMed: 23407358]
56. Humphrey W, Dalke A & Schulten K VMD: visual molecular dynamics. *J Mol Graph* 14, 33–8, 27–8 (1996). [PubMed: 8744570]
57. Shevchenko A, Tomas H, Havlis J, Olsen JV & Mann M In-gel digestion for mass spectrometric characterization of proteins and proteomes. *Nat Protoc* 1, 2856–60 (2006). [PubMed: 17406544]
58. Cox J & Mann M MaxQuant enables high peptide identification rates, individualized p.p.b.-range mass accuracies and proteome-wide protein quantification. *Nat Biotechnol* 26, 1367–72 (2008). [PubMed: 19029910]
59. Olsen JV & Mann M Improved peptide identification in proteomics by two consecutive stages of mass spectrometric fragmentation. *Proc Natl Acad Sci U S A* 101, 13417–22 (2004). [PubMed: 15347803]

60. MacLean B et al. Skyline: an open source document editor for creating and analyzing targeted proteomics experiments. *Bioinformatics* 26, 966–8 (2010). [PubMed: 20147306]

Author Manuscript

Author Manuscript

Author Manuscript

Author Manuscript

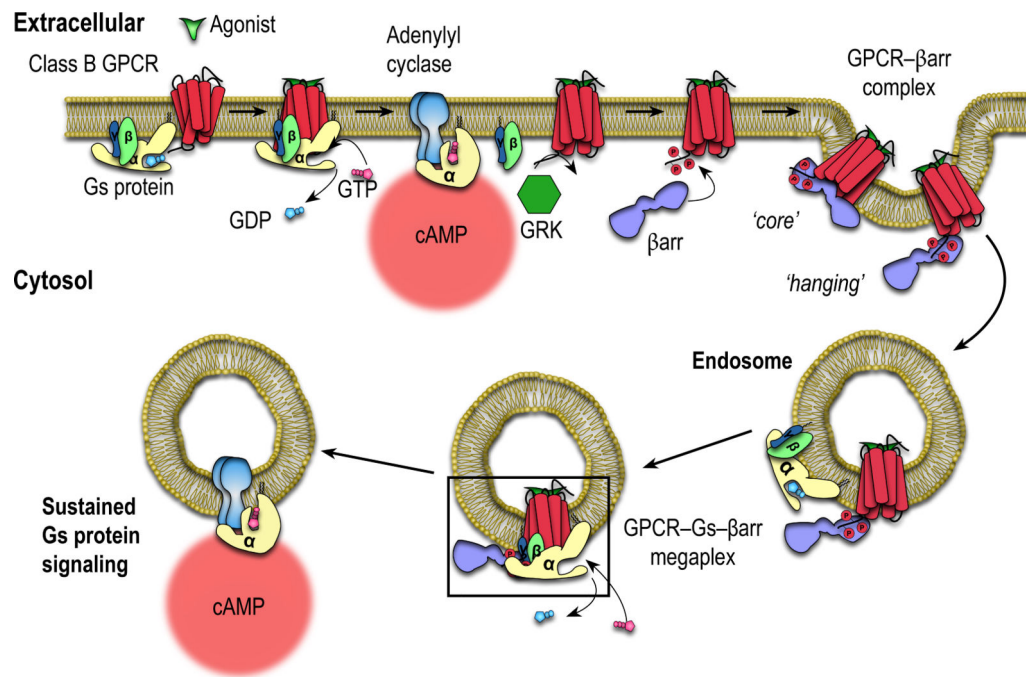


**Fig. 1. Schematic illustration of the mechanism of sustained signaling through the formation of endosomal class B GPCR-G protein-βarr megacomplexes.** Binding of β-arrestin (βarr) to a GRK-phosphorylated GPCR tail (leaving the receptor intracellular core open) and subsequent receptor internalization allows for further G protein binding, forming a megaplex (black box). The megaplex continues to activate G protein, leading to sustained endosomal cAMP generation.

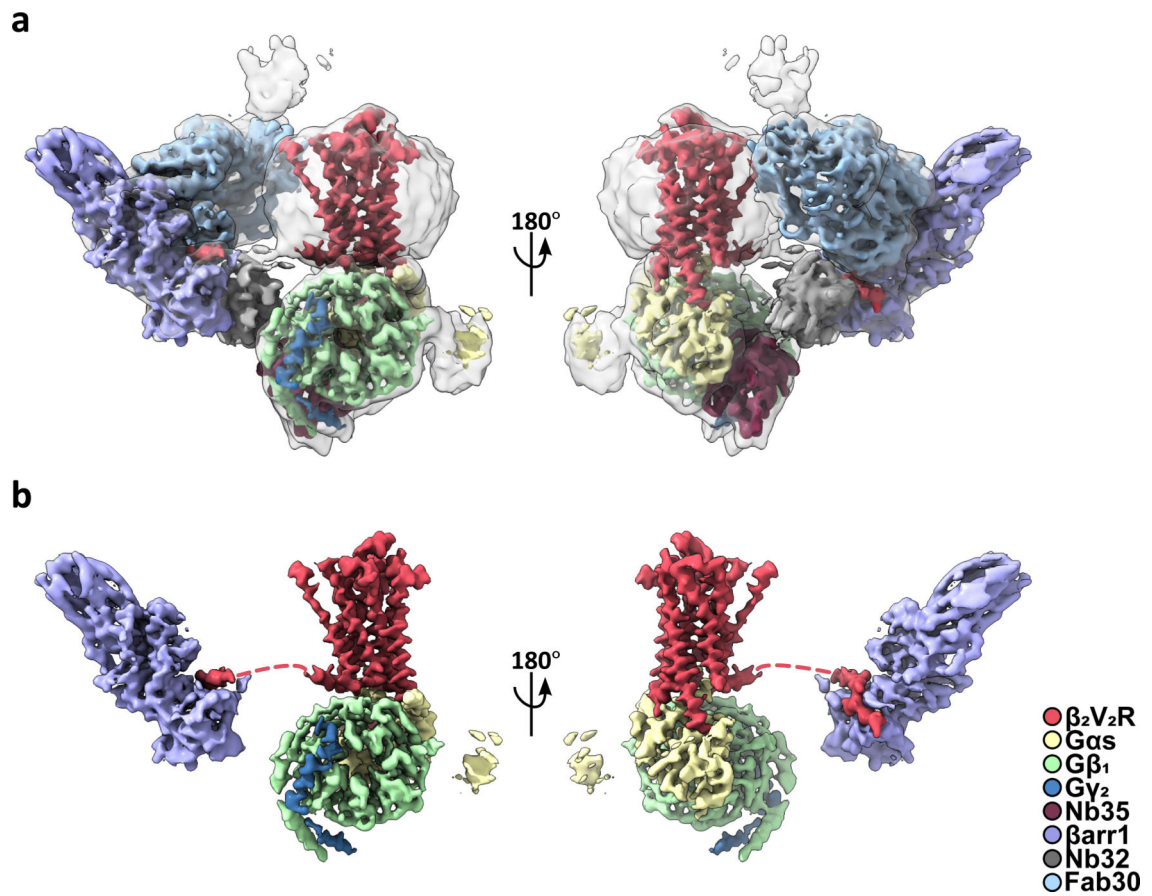


**Fig. 2. Cryo-EM structure of a  $\beta_2V_2R$ -Gs- $\beta arr1$  megaplex.**

**a.** Composite cryo-EM density map of the megaplex reconstruction fitted into a transparent envelope of the megaplex consensus structure. **b.** Same as in **a**, but with protein stabilizers (Nb35, Nb32, and Fab30) and consensus reconstruction removed. Red dashed lines indicate the flexible C-terminal tail connecting  $\beta arr1$  to the receptor.

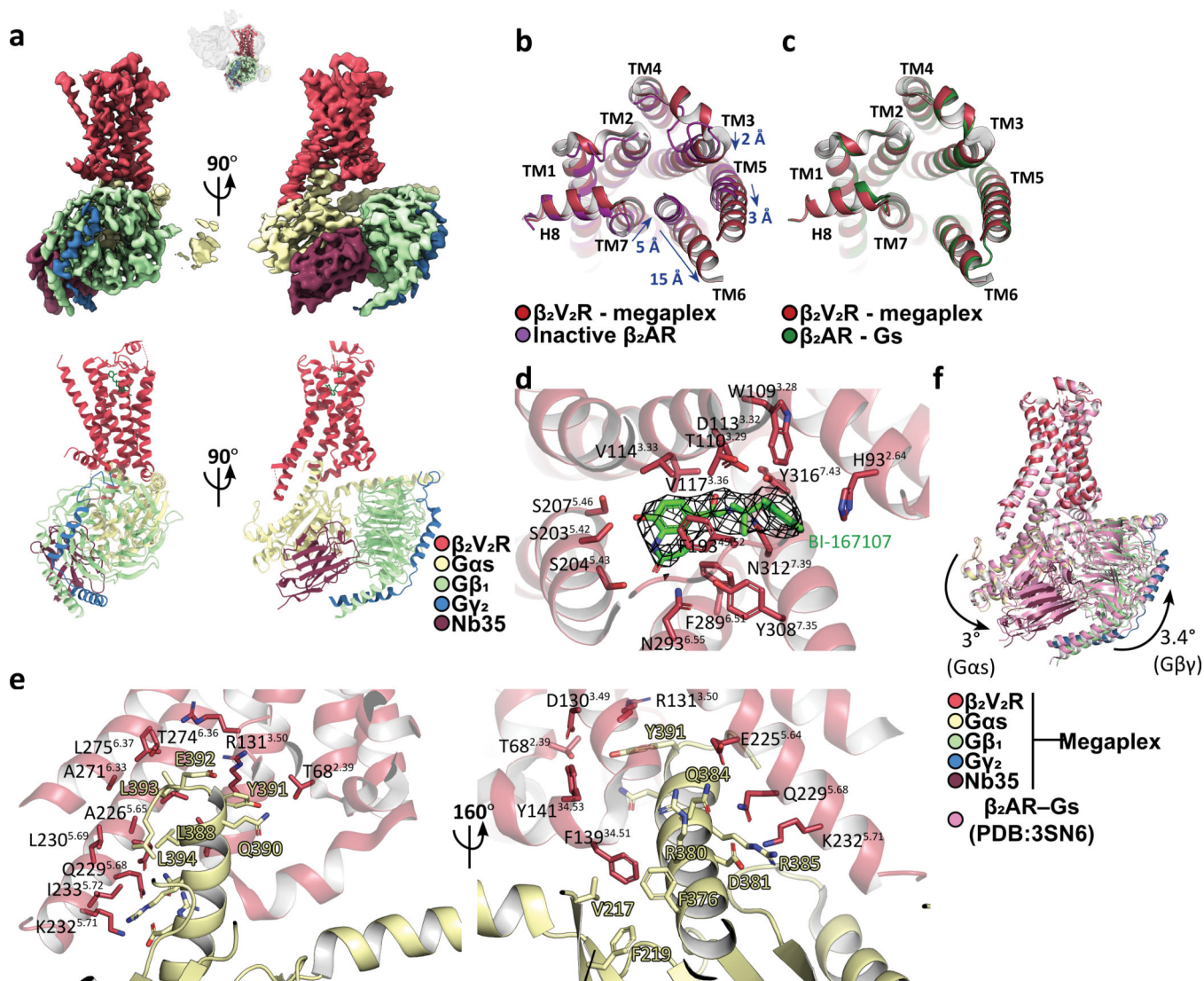


**Fig. 3. Structure and interactions of the  $\beta_2V_2R$ -Gs portion of the megaplex**  
**a.** Orthogonal views of the density map and model for the  $\beta_2V_2R$ -Gs portion of the megaplex. Small top image orients the  $\beta_2V_2R$ -Gs subcomplex in relation to the megaplex consensus structure. **b.** Intracellular view of the superimposition between the megaplex  $\beta_2V_2R$  and the inactive, carazolol-bound  $\beta_2AR$  (PDB: 2RH1). Blue arrows indicate movements in transmembrane helices (TMs) 3,5,6 and 7 and their magnitudes. **c.** Intracellular view of the superimposition between the megaplex  $\beta_2V_2R$  and the Gs-bound  $\beta_2AR$  (PDB: 3SN6). **d.** Ligand-binding pocket of the  $\beta_2V_2R$ , with density for the agonist BI-167107 (BI-167107, green) in mesh. **e.** Interaction of the  $\alpha_5$ -helix of G $\alpha_s$  with hydrophobic residues on TM5 and TM6, and with polar residues between TM3 and TM5 of the  $\beta_2V_2R$ .  $\beta_2V_2R$  residues are labeled in black for **d** and **e**. **f.** Structural comparison of the  $\beta_2AR$ -Gs complex (pink, PDB: 3SN6) against the  $\beta_2V_2R$ -Gs portion of the megaplex, both aligned by their receptors. Curved arrows indicate 3° rotation of G $\alpha_s$  around an axis parallel to the  $\beta_2V_2R$ - $\alpha_5$  helix contact and 3.4° rotation of G $\beta\gamma$  around an axis parallel to the plasma membrane seen in the megaplex.

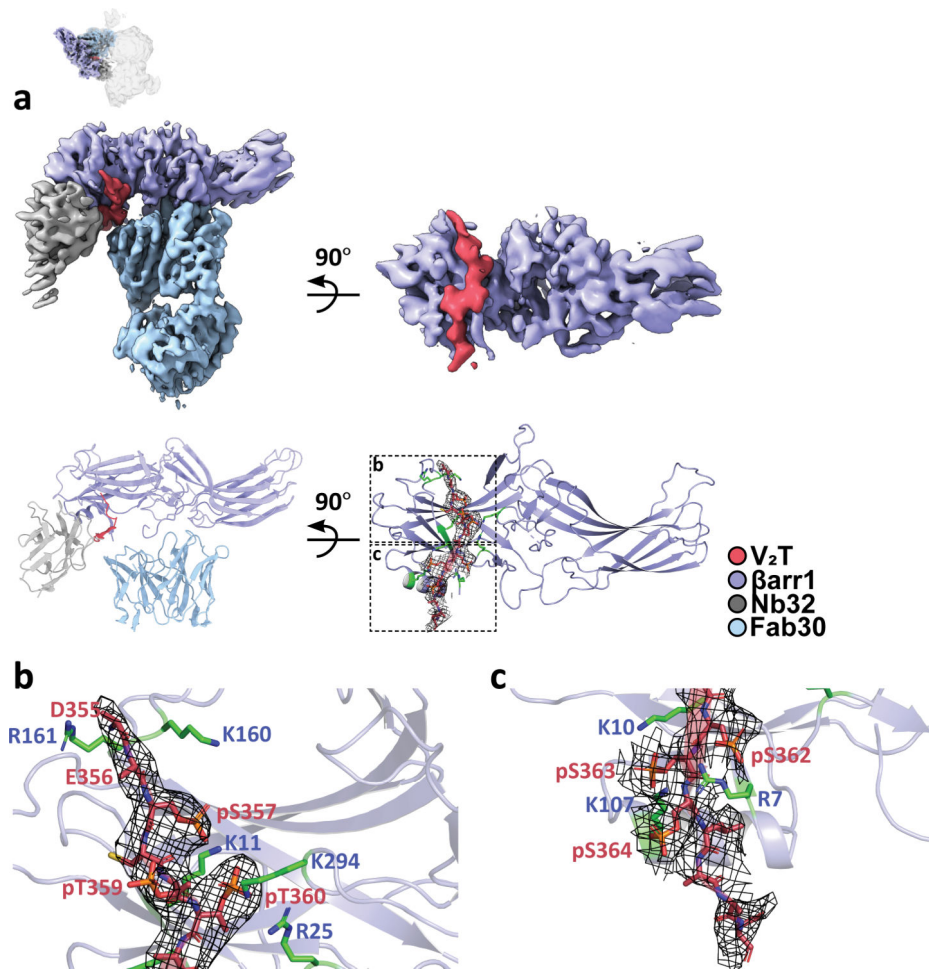


**Fig. 4. Structure and interactions of the  $\beta$ arr1-V<sub>2</sub>T portion of the megaplex.**  
**a**, Density map and model for the megaplex  $\beta$ arr1-V<sub>2</sub>T. Mesh delineates density for the V<sub>2</sub>T. Small top image orients the  $\beta$ arr1-V<sub>2</sub>T subcomplex in relation to the megaplex consensus structure. **b,c**, Regions of the V<sub>2</sub>T with phosphorylated residues pS357, pT359, pT360 (**b**) and pS362, pS363, and pS364 (**c**) interacting with positively charged residues on  $\beta$ arr1, which are colored in green and labeled in blue.

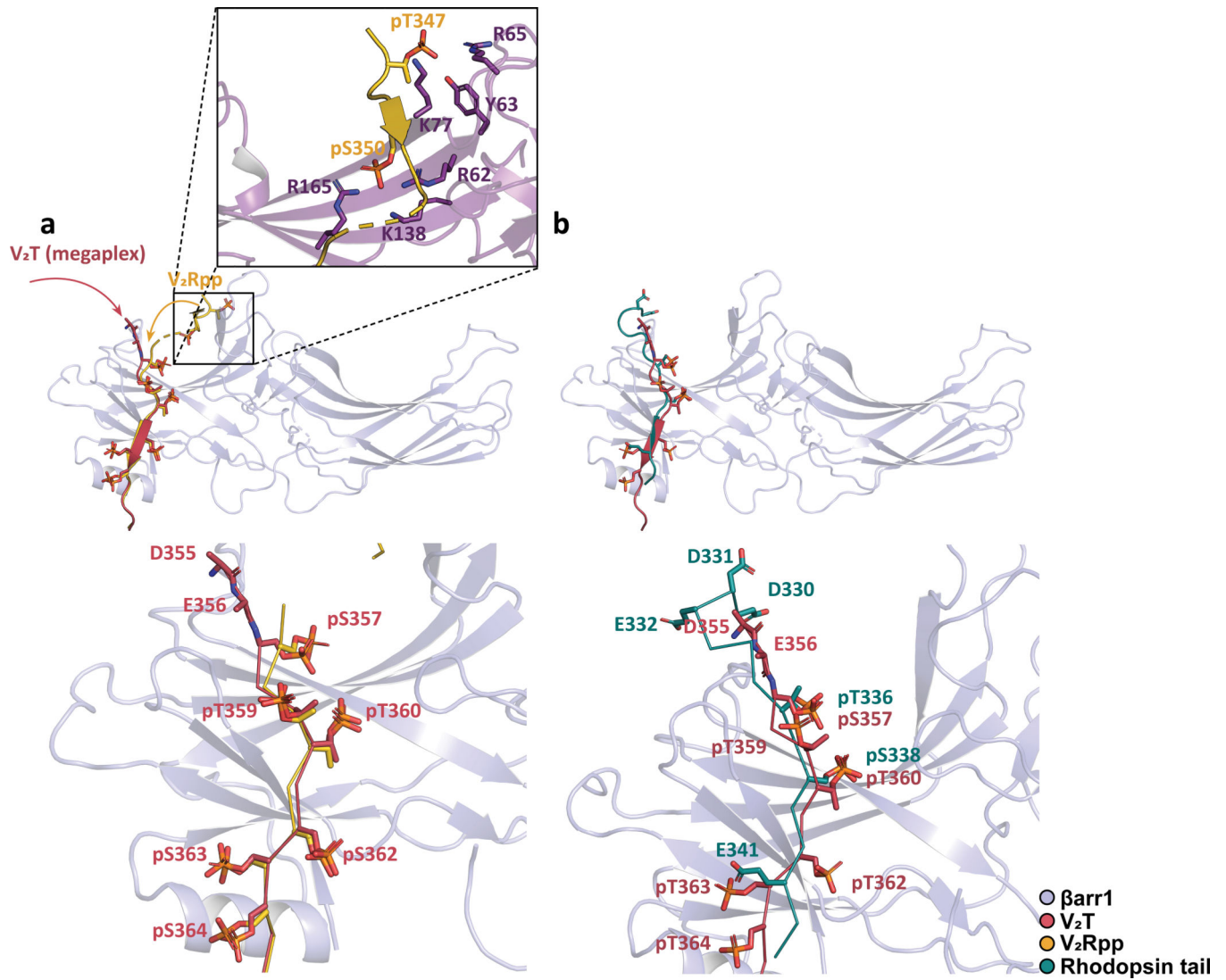


**Fig. 5. Comparison of the megaplex  $\beta$ arr1-V<sub>2</sub>T to the V<sub>2</sub>Rpp- $\beta$ arr1-Fab30 and rhodopsin-visual arrestin crystal structures.**

**a.** Superimposition between the  $\beta$ arr1-V<sub>2</sub>T (megaplex) and the V<sub>2</sub>Rpp- $\beta$ arr1-Fab30 crystal structure. Inset shows interaction between pT347 and pS350 of the V<sub>2</sub>Rpp with residues near the finger loop region of  $\beta$ arr1. Red and yellow arrows delineate the differing path of the V<sub>2</sub>T and V<sub>2</sub>Rpp, respectively. **b.** Alignment between  $\beta$ arr1-V<sub>2</sub>T (megaplex) and the rhodopsin-visual arrestin crystal structure. For clarity, only  $\beta$ arr1 of the megaplex is shown in **a** and **b**.

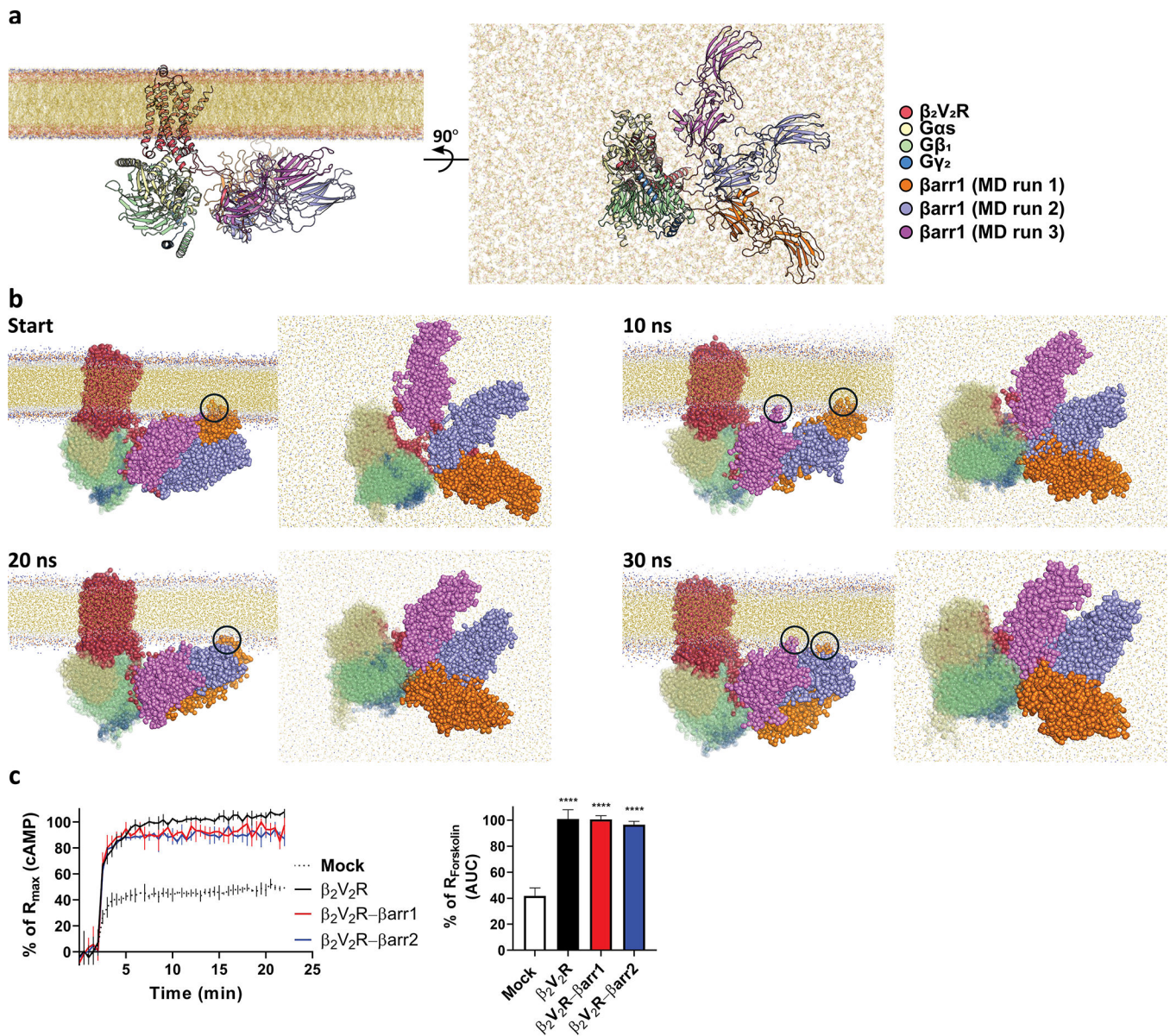


**Figure 6. The megaplex within a membrane environment.**

**a**, Orthogonal views of three modeled megaplex structures for molecular dynamics (MD) simulations with differing  $\beta arr1$ - $V_2T$  positions, aligned by their  $\beta_2V_2R$ -Gs region. **b**, Coarse-grained MD models of the three structures, aligned by their  $\beta_2V_2R$ -Gs region at 10 ns increments. Black circles denote transient contact between  $\beta arr1$  residues and the lipid bilayer. **c**, Real-time cAMP measurement of BI-stimulated  $\beta_2V_2R$  or  $\beta_2V_2R$ - $\beta arr1/2$  in  $\beta_2AR/\beta arr1/\beta arr2$  triple knock-out HEK293 cells, expressed as percentages of 10  $\mu M$  Forskolin control. Data represents mean  $\pm$  S.E.M. of four independent experiments for the  $\beta_2V_2R$ - $\beta arr1$  and  $\beta_2V_2R$ - $\beta arr2$  conditions and of three independent experiments for the  $\beta_2V_2R$  condition. Ordinary one-way ANOVA with Holm-Sidak's multiple comparison post-

hoc test was performed to determine statistical significance between mock control and the  $\beta_2V_2R$  or  $\beta_2V_2R$ - $\beta$ arr1/2 conditions (\*\*\*\* $P < 0.0001$ ).

Author Manuscript

Author Manuscript

Author Manuscript

Author Manuscript

**Table 1.**

Cryo-EM data collection, refinement and validation statistics

	Megaplex Consensus Reconstruction (EMD-9377)	$\beta_2V_2R$ -Gs (EMD-9376, PDB 6NI3)	$\beta_{arr1}$ -V <sub>2</sub> T (EMD-9375, PDB 6NI2)
<b>Data collection and processing</b>			
Magnification	105,000	105,000	105,000
Voltage (kV)	300	300	300
Electron exposure ( $e^-/\text{\AA}^2$ )	104.3	104.3	104.3
Defocus range ( $\mu\text{m}$ )	1.0–3.5	1.0–3.5	1.0–3.5
Pixel size ( $\text{\AA}$ )	1.04	1.04	1.04
Symmetry imposed	C1	C1	C1
Initial particle images (no.)	8.15 million	8.15 million	8.15 million
Final particle images (no.)	317,529	299,893	230,021
Map resolution ( $\text{\AA}$ )	4.8	3.8	4.0
FSC threshold	0.143	0.143	0.143
Map resolution range ( $\text{\AA}$ )	7–12	3.5–7	3.5–7
<b>Refinement</b>			
Initial model used (PDB code)		3SN6	4JQI
Model resolution ( $\text{\AA}$ )		4.15	4.37
FSC threshold		0.5	0.5
Model resolution range ( $\text{\AA}$ )			
Map sharpening <i>B</i> factor ( $\text{\AA}^2$ )	–202.3	–133.6	–139.0
<b>Model composition</b>			
Nonhydrogen atoms		8136	5381
Protein residues		1043	704
Ligands		1	0
<b><i>B</i> factors (<math>\text{\AA}^2</math>)</b>			
Protein		83.75	131.66
Ligand		74.16	
<b>R.m.s. deviations</b>			
Bond lengths ( $\text{\AA}$ )		0.01	0.009
Bond angles ( $^\circ$ )		1.197	1.297
<b>Validation</b>			
MolProbity score		1.6	1.81
Clashscore		4.67	6.6
Poor rotamers (%)		0.23	0
<b>Ramachandran plot</b>			
Favored (%)		94.83	93.11
Allowed (%)		5.17	6.74
Disallowed (%)		0	0.15